



**HAL**  
open science

# Efficient $^{23}\text{Na}$ triple-quantum signal imaging on clinical scanners -CaRtesian Imaging of Single and Triple-Quantum $^{23}\text{Na}$ (CRISTINA)

Michaela Au Hoesl, Lothar Schad, Stanislas Rapacchi

► **To cite this version:**

Michaela Au Hoesl, Lothar Schad, Stanislas Rapacchi. Efficient  $^{23}\text{Na}$  triple-quantum signal imaging on clinical scanners -CaRtesian Imaging of Single and Triple-Quantum  $^{23}\text{Na}$  (CRISTINA). *Magnetic Resonance in Medicine*, 2020, 10.1002/mrm.28284 . hal-02861102

**HAL Id: hal-02861102**

**<https://amu.hal.science/hal-02861102v1>**

Submitted on 8 Jun 2020

**HAL** is a multi-disciplinary open access archive for the deposit and dissemination of scientific research documents, whether they are published or not. The documents may come from teaching and research institutions in France or abroad, or from public or private research centers.

L'archive ouverte pluridisciplinaire **HAL**, est destinée au dépôt et à la diffusion de documents scientifiques de niveau recherche, publiés ou non, émanant des établissements d'enseignement et de recherche français ou étrangers, des laboratoires publics ou privés.



Distributed under a Creative Commons Attribution - NonCommercial - NoDerivatives 4.0 International License

# Efficient $^{23}\text{Na}$ triple-quantum signal imaging on clinical scanners – CaRtesian Imaging of Single and Triple-Quantum $^{23}\text{Na}$ (CRISTINA)

Michaela AU Hoesl MS<sup>1</sup>, Lothar R Schad PhD<sup>1,\*</sup>, Stanislas Rapacchi PhD<sup>2,\*</sup>

<sup>1</sup> Computer Assisted Clinical Medicine, Heidelberg University, 68167 Mannheim, Germany

<sup>2</sup> Aix-Marseille Univ, CNRS, CRMBM, Marseille, France

\* Author Lothar R Schad and Author Stanislas Rapacchi contributed equally to this work

## Acknowledgements

This article is based in parts upon work from COST Action “CA16103 Assessment of Kidney Physiology using  $^{23}\text{Na}$  triple quantum spectroscopy”, supported by COST (European Cooperation in Science and Technology).

This work was performed by a laboratory member of France Life Imaging network (grant ANR-11-INBS-0006). This work was performed on the platform 7T-AMI, a French “Investissements d’Avenir” programme” (grant ANR-11-EQPX-0001).

## ABSTRACT

**PURPOSE** To capture the multi-quantum coherence (MQC) sodium signal. Different phase-cycling options and sequences are compared in a unified theoretical layout, and a novel sequence is developed.

**THEORY and METHODS:** An open-source simulation overview is provided (<https://github.com/MHoesl/>) with graphical explanations to facilitate MQC understanding and access to techniques. Biases such as B0 inhomogeneity and stimulated echo (STE) signal were simulated for four different phase-cycling options previously described. Considerations for efficiency and accuracy lead to the implementation of a 2D Cartesian Single and Triple quantum Imaging of  $^{23}\text{Na}$  (CRISTINA) sequence employing two 6-steps cycles in combination with a multi-echo readout. CRISTINA capabilities were assessed on an 8x60ml, 0%–5% agarose phantom with 50mM–154mM  $^{23}\text{Na}$  concentration at 7T. CRISTINA was demonstrated subsequently in vivo in the brain.

**RESULTS** Simulation of B0 inhomogeneity showed severe signal drop out, which can lead to erroneous MQC measurement. STE signal was highest at the time of TQC signal maximum. However, STE signal is separated by Fourier Transform as an offset and did not interfere with MQC signals. The multi-echo readout enabled capturing both SQC and TQC signal evolution at once. Signal combination of two phase-cycles with a corresponding B0 map was found to recover the signal optimally. Experimental results confirm and complement the simulations.

**CONCLUSION** CRISTINA captures TQC and SQC signal evolution to provide  $T2^*$ fast and  $T2^*$ slow maps by fitting as well as the optimal measurement of TQC signal and extrapolation of SQC signal to  $TE=0\text{ms}$ . Sodium concentration maps can be estimated.

**Key words:**  $^{23}\text{Na}$  MRI, sodium triple-quantum imaging, multiple-quantum coherence transfer pathways

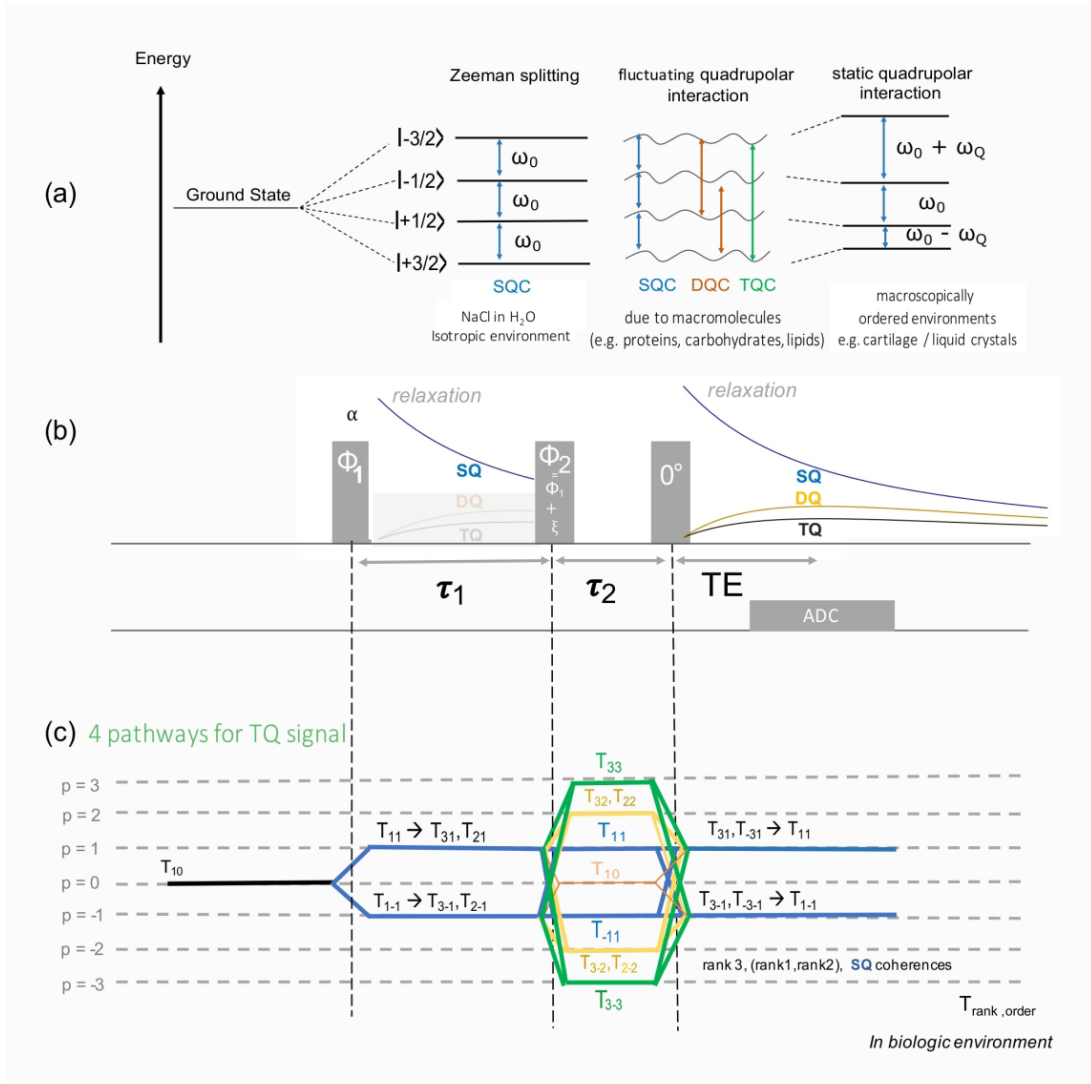


**Figure1:** (a) (<sup>23</sup>Na) spin 3/2 nuclei interaction with a magnetic field: In isotropic environment, the ground state splits into the 4 different energy levels with equidistant levels. In biologic environment fluctuating quadrupolar interaction leads to the observation of DQC and TQC. Static quadrupolar interaction in ordered environments is rare in biological medium. (b) the three pulses experiment used to achieve multi quantum coherence (MQC) transfer (c) coherence transfer diagram for pathways that can be probed. Relaxation between the first and second pulse,  $\tau_1$ , is crucial for TQC creation. The time between the second and third pulse ( $\tau_2$ ) is chosen as short as possible to limit MQC signal loss. The tensor  $T_{\text{rank,order}}$  changes its order after each RF pulse whereas only relaxation and quadrupolar coupling change the rank of the tensor. In perfect quadrature detection, only coherence level of -1 is observable. However, imperfect quadrature detection is common in MRI and signals can end up in the +1 pathway as well.

## Option II: 2x8 steps

$$\Delta\phi = \pi/4$$

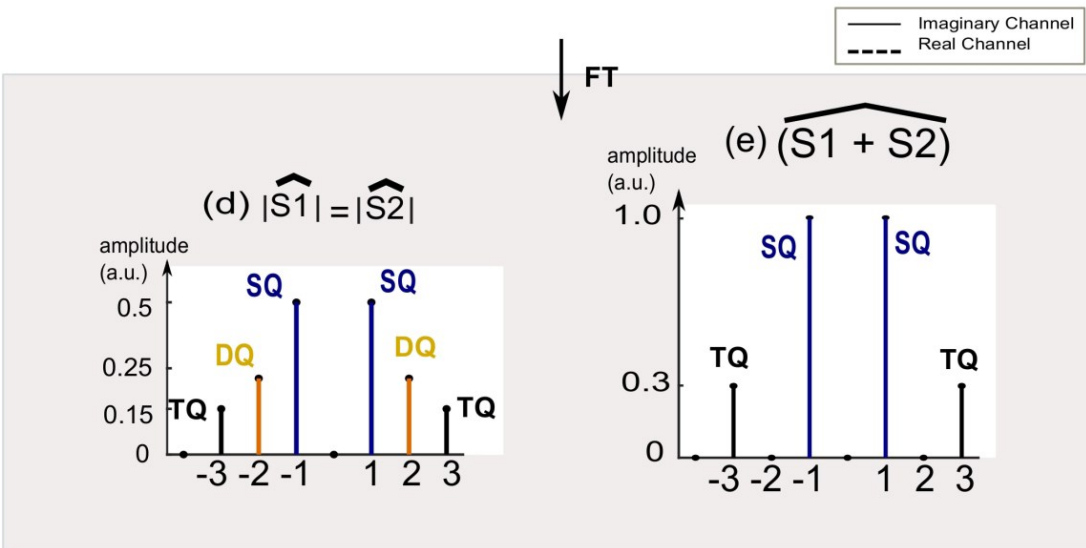
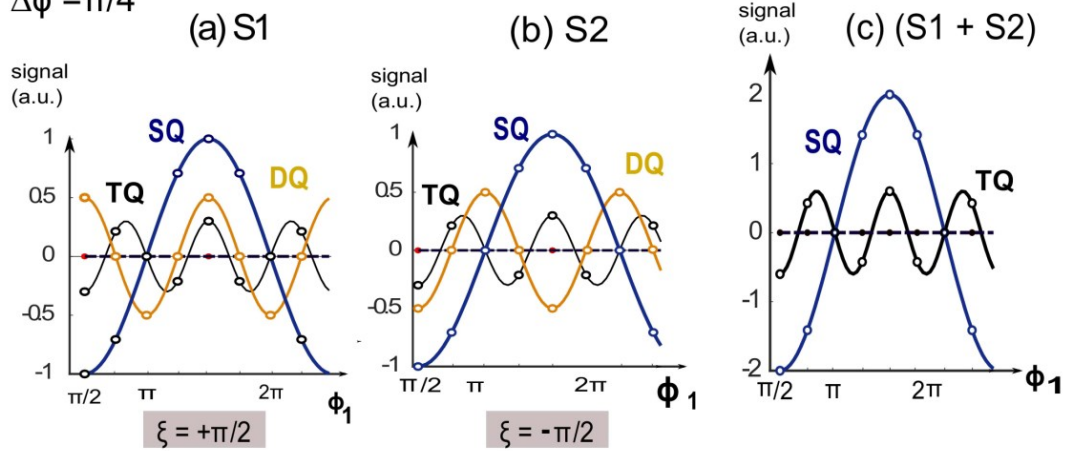
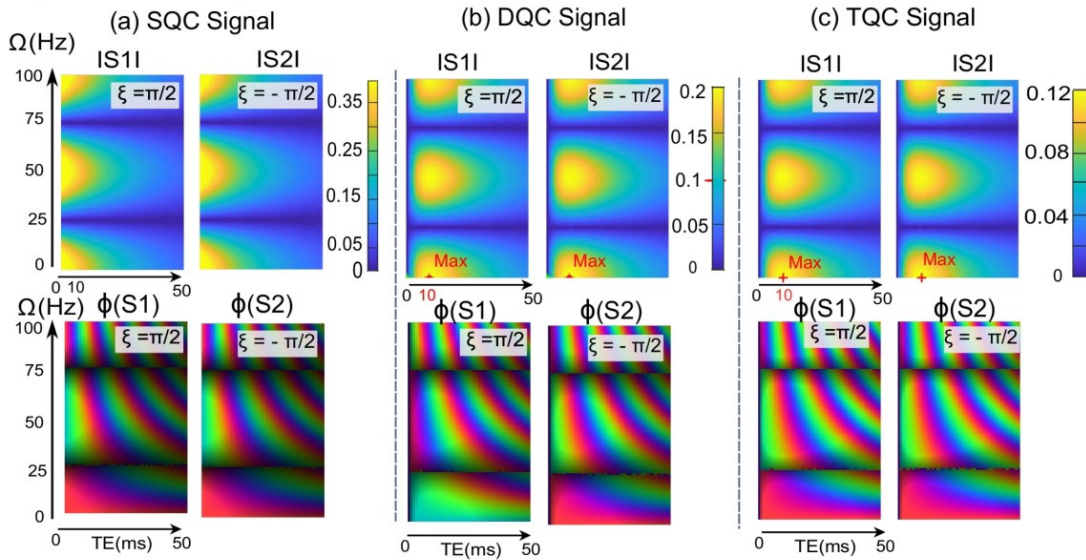


**Figure 2: Option II: TQ(T)PPI phase cycling.** The SQC and DQC are optimally sampled however the TQC maximum is only sampled at 2 out of 8 points. Evolution time increment and relaxation have been discarded. The sum of the two cycles signals effectively cancels out DQC signal. In the resulting spectra the DQC cancellation can be observed, and oversampling leads to TQC being split in 2 components.

**Option II: 2x8 steps**



(d) Spectra  $\hat{S}$  along echo time (TE), at  $\Omega = 0$  Hz

(e) Spectra  $\hat{S}$  along B0 offset, at TE = 10 ms

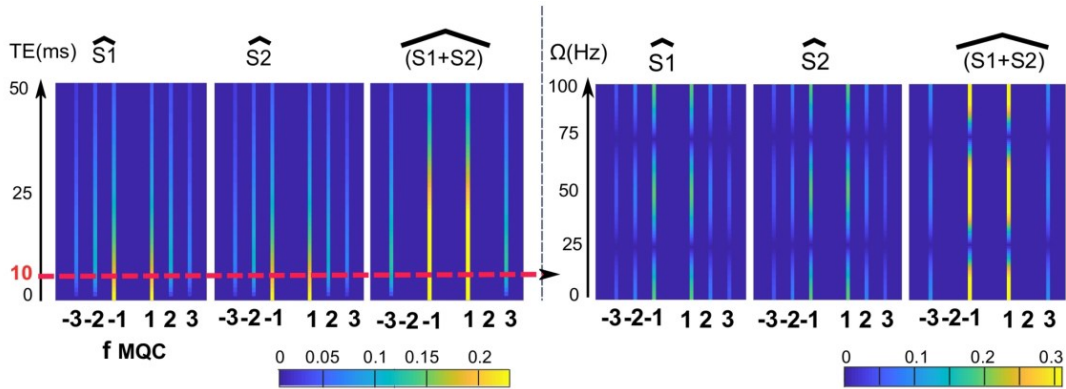


**Figure 3: Option III: Fleysher cycles for recovering B0 offset bias.** Their addition and subtraction  $\hat{S}_+ \hat{S}_-$ , in combination with a reverse of the known B0 offset, results in the recovered spectrum (e). The amplitudes in e) are the initially set values for the simulation which shows that the signal was effectively recovered, independently of the B0 offset.

**Option III: 2x6 steps  $\Delta\phi = \pi/3$**

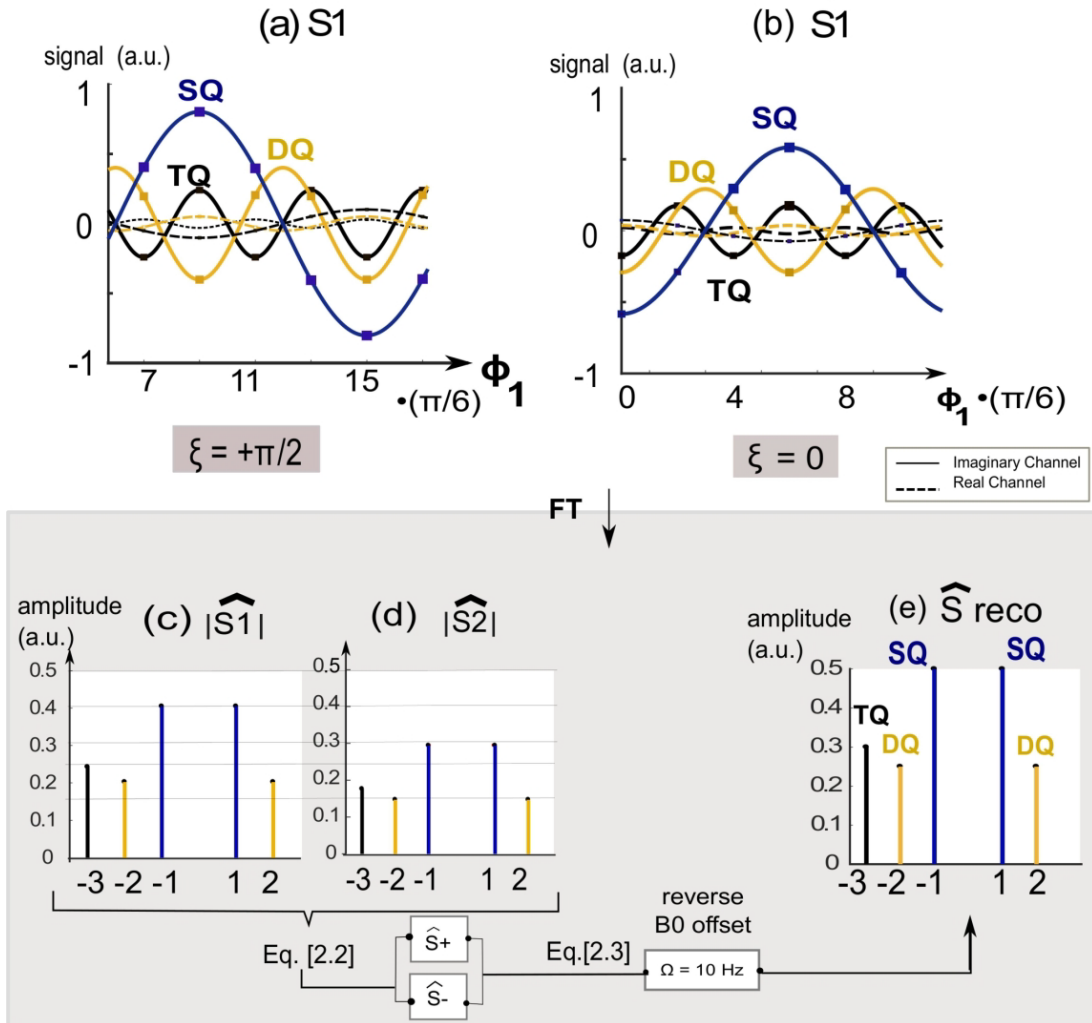


**Figure 4:** Option II TQ(T)PPI simulation including relaxation and B0 offset. The magnitude and phase of the signals at  $\phi_0$  are shown independently for the three quantum coherences, (a)SQC, (b)DQC and (c)TQC. The complex DQC signal (Row II.) shows signal cancellation due to opposite phases for the two phase-cycles. For the SQC and TQC signals, signal addition is constructive. (d) and (e) show the spectra for the individual phase cycles ( $\xi = \pm \frac{\pi}{2}$ ) as well as for the added signals in (d) along the B0 offset and (e) along the echo time. Signal cancellation at 25Hz and 75Hz can be observed.

**Option III: 2x6 steps**

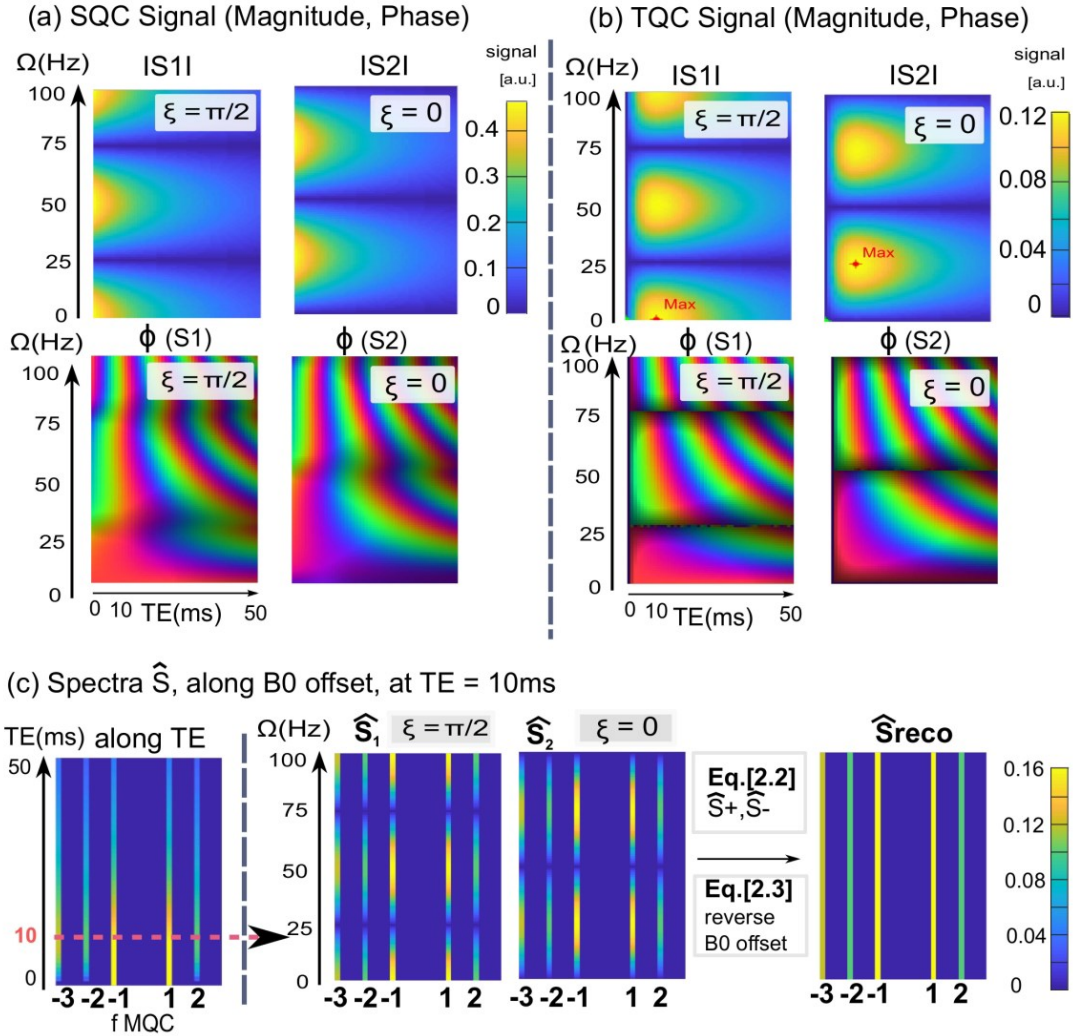
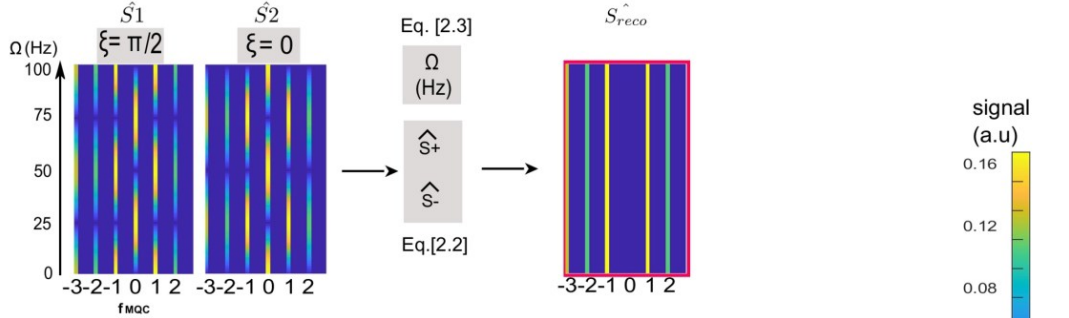


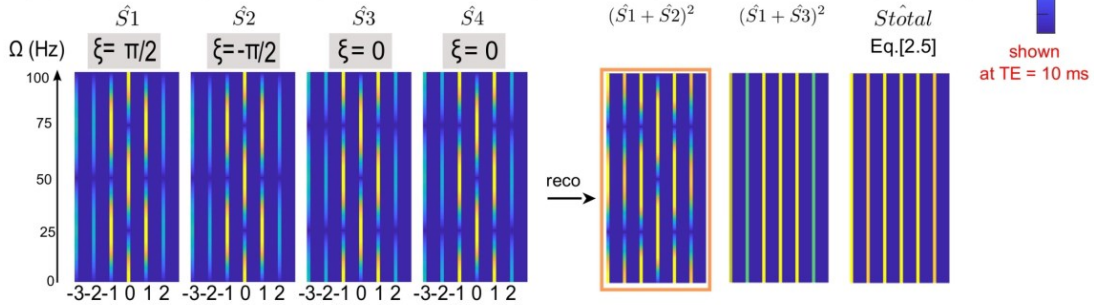
**Figure 5:** Option III, Fleysher cycles, along echo time (0ms to 50ms) and varying B0 offset from 0Hz up to 100Hz: Magnitude and phase signal are shown for the SQC and TQC to show the differing oscillation due to B0 offset. This offers the possibility of signal reconstruction, shown in the spectra data in (c). Signal evolution with differing signal maxima of SQC and TQC signal along echo time is given for no B0 offset. Then the spectra are given at TE = 10ms along a B0 offset from 0 to 100Hz. Signal vanishing can be observed at 25 Hz and 75 Hz offset in the first cycle and at 0, 50 and 100 Hz in the second cycle. The reconstructed spectrum is independent of the B0 field offset.



**(a) Option III & V (Fleysher, CRISTINA) : complete signal in 2 cycles**



**(b) Option IV (SISTINA): incomplete signal using cycles 1 and 2 (*in vivo*)**



**(c) Experimental results with linear off-resonance**

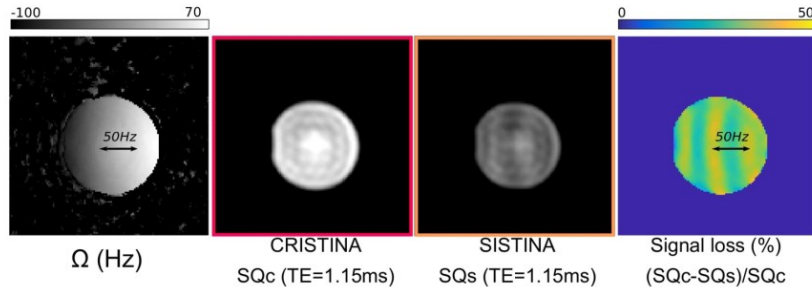


**Figure 6: I:** SQC and Stimulated echo (SE) signal for varying echo time (TE) from 0ms to 30ms (x-axis) and varying B0 offset from 0 to 100Hz (y-axis). (a) SQ Signal without SE signal bias, (b) shows only the SE signal, with the expected maximum at 10ms which coincided with the set evolution time  $\tau_1$  (c) SQ signal with SE signal bias, for varying echo time (TE) from 0ms to 30ms (x-axis) and varying B0 offset from 0 to 100Hz (y-axis).

II: Option III phase cycle choice under STE and B0 offset bias: STE signal bias is visible at the zero-frequency position in Fourier domain, at echo time TE 10 ms and varies along B0 offset in the independent two cycles. B0 offset from 0 to 100Hz (y-axis). (e) Reconstruction using B0 values lead to full recovery with no STE offset. (f) The sum of squares reconstruction did not remove the STE offset. III: Option IV, SISTINA phase cycles simulated with STE signal bias. On the right of the arrow the spectra were reconstructed from the data (a-d) (e) magnitude reconstruction of S1 and S2. (f) magnitude reconstruction of S1 and S3 (g) magnitude reconstruction of all four contributions. STE signal was not removed in the reconstructions and still visible in the zero frequency.(e) choosing the two first phase cycles keeps the B0 inhomogeneity bias.

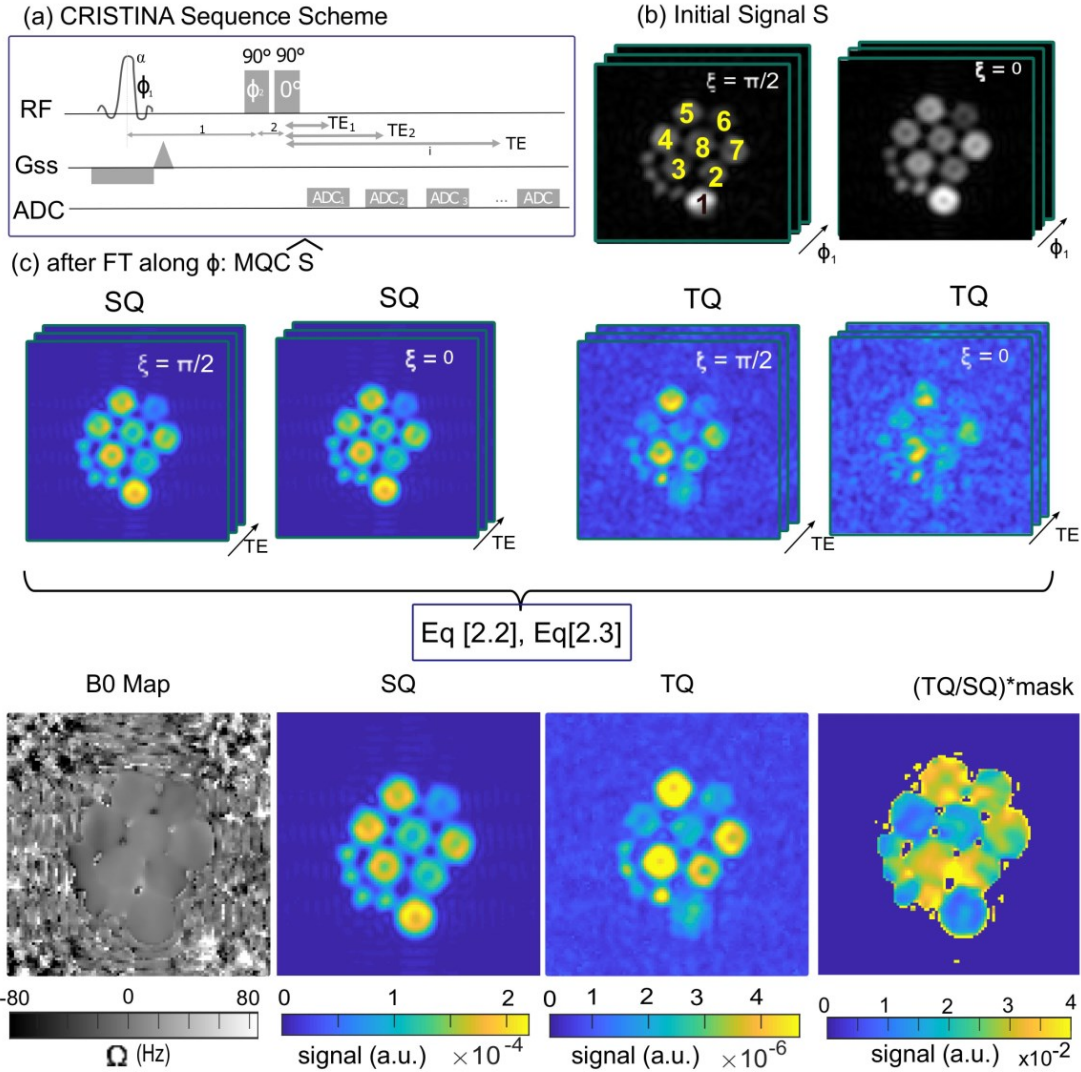


**Figure 7:** (a) 2D multi-echo sequence scheme (b) initial phase cycle signal image at  $\Phi_{1,t=0}$  (d) from the phase cycle data, the spectroscopic images were reconstructed by voxel wise FT, for each TE set.  $\hat{S}^+$  and  $\hat{S}^-$  were calculated. The B0 map was calculated from quadrature combination of the two cycles and the multi TE experiment. Using the voxel wise B0 offset values, the total spectroscopic result,  $\hat{S}_{total}$ , was reconstructed. A complex signal depiction of a voxel of interest, in phantom 5 can be found in the supporting information Figure S.2.

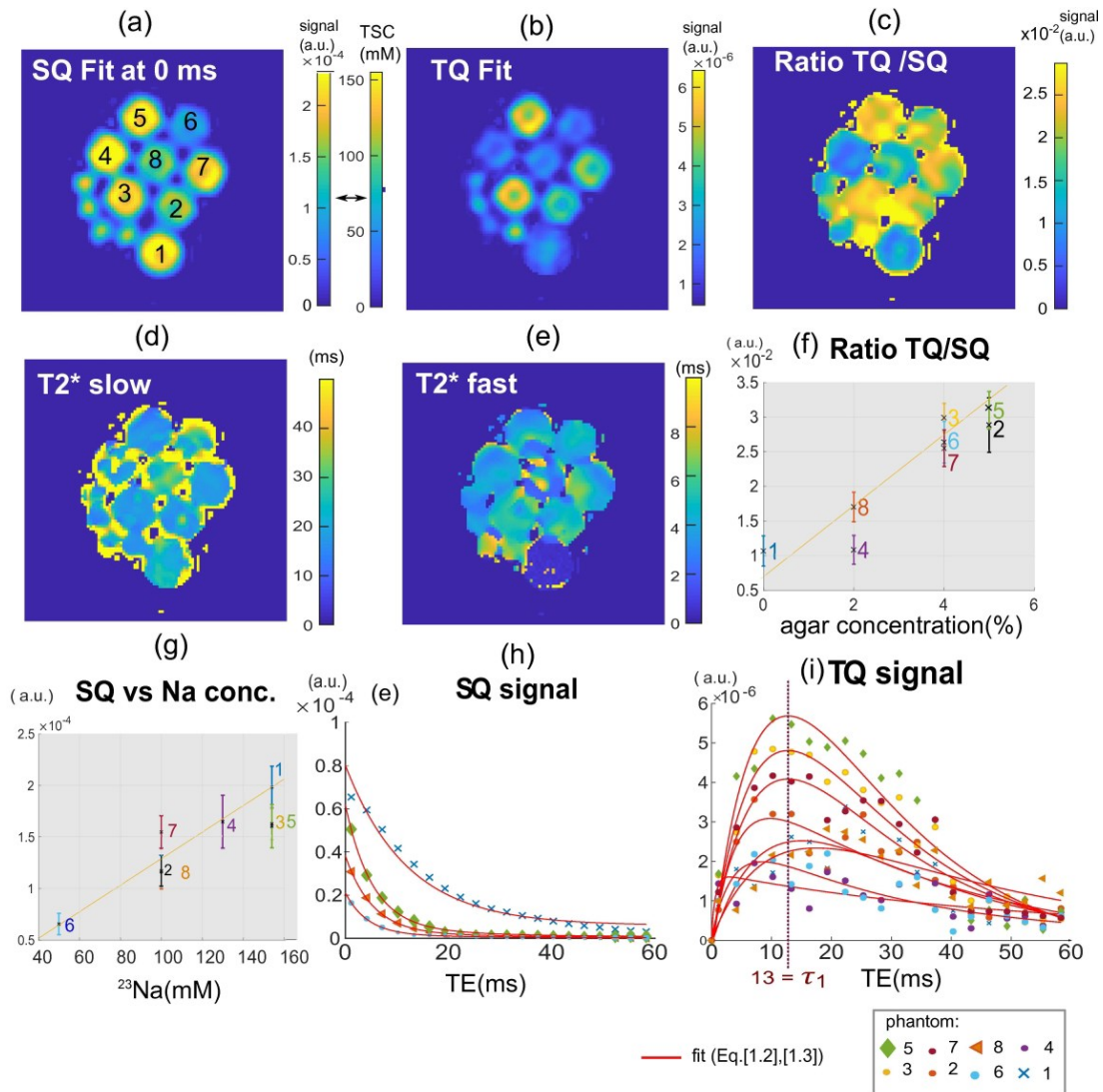


**Figure 8:** (a) fitted SQ signal, extrapolated to TE = 0ms. The colorbars show the signal strength and the sodium concentration in mM by a linear fit using the (2%, 130mM and 100mM) phantoms for calibration. Phantoms are numbered for the following. (b) TQ signal at TE 13.3 ms with higher signal strength in phantoms 3 and 5 (4%, 5% agar, 154mM). (c) TQ to SQ ratio relates to agar values, independent of sodium content (d,e) T2\* slow and T2\*fast maps by voxel wise fit. The liquid phantom 1 showed a mono-exponential result and therefore has values close to zero. (f) TQ to SQ ratio is visualized against agar concentration and showed a linear relationship ( $R^2 = 0.87$ ). (g) SQ signal at TE = 0ms showed a linear relationship to sodium concentration ( $R^2 = 0.75$ ). Values in f,g were evaluated and averaged over the tube size. (h) SQ signal over echo time and fit, only four phantoms, different in agar and sodium concentration, are depicted to ease visual comparison. (i) TQ signal over echo time and fit. Table S.3 with T2 slow and T2 fast values, along with the concentrations of each of the numbered phantoms, can be found in the supporting information.

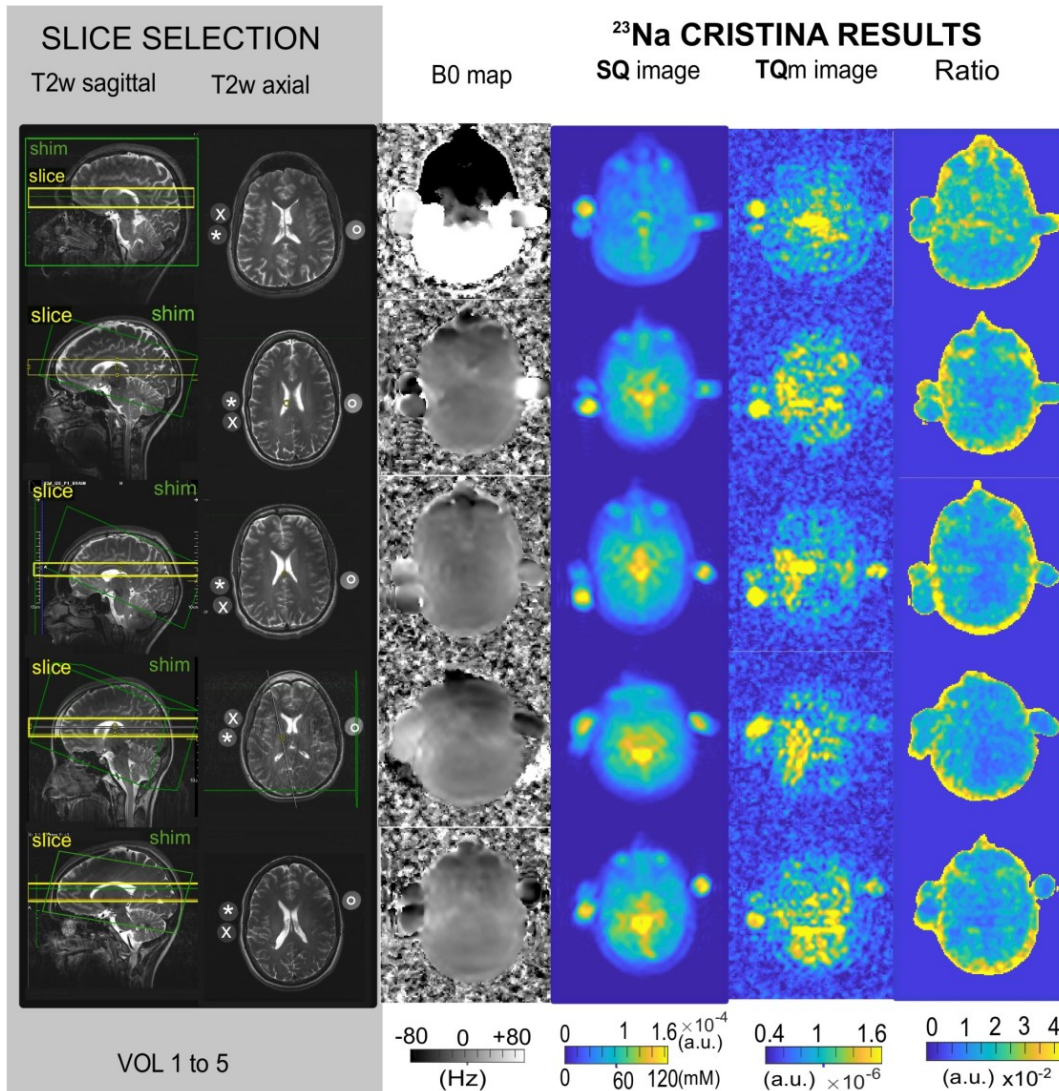


**Figure 9:** (a,b) T2w image and the 2D slice position for the sodium acquisition in coronal and axial view (c) initial phase cycle signal at  $\Phi_{1,t=0}$  for the first cycle (d) reconstructed SQ image for the first cycle. (e,f) TQ images for both cycles. (g) B0 map leading to the total spectroscopic signal,  $\hat{S}_{total}$ . To enhance SNR the TQ images are averaged from the 2<sup>nd</sup> to the 7<sup>th</sup> echo which equals the echo times from 4ms to 18ms.

	phase cycles	$\Delta\phi_1$		$\phi_{1,t=0}$	$\xi = (\phi_2 - \phi_1)$	Acronym
<b>Option I</b>	1x6-steps	$\pi/3$	one cycle	$\pi/6$	$\pi/2$	'original' <sup>1</sup>
<b>Option II</b>	2x8-steps	$\pi/4$	1 <sup>st</sup> cycle	$\pi/2$	$\pi/2$	'TQ(T)PPI' <sup>19,20</sup>
			2 <sup>nd</sup> cycle	$\pi/2$	$-\pi/2$	
<b>Option III</b>	2x6-steps	$\pi/3$	1 <sup>st</sup> cycle	$\pi/2$	$\pi/2$	'Fleysher' <sup>26</sup>
			2 <sup>nd</sup> cycle	0	0	
<b>Option IV</b>	4x6-steps	$\pi/3$	In-vivo cycles	$\pi/6$	$\pi/2$	'SISTINA' <sup>22</sup>
				$7\pi/6$	$-\pi/2$	
			Phantom cycles	$2\pi/3$	0	
<b>Option V</b>	2x6-steps	$\pi/6$	1 <sup>st</sup> cycle	$\pi/2$	$\pi/2$	'CRISTINA'
			2 <sup>nd</sup> cycle	0	0	

Table 1: Overview over the highlighted phase-cycle options

## INTRODUCTION

Multi-quantum sodium NMR has already been investigated and described 3 decades ago<sup>1-5</sup>. Recently, technological advances have led to a revival of sodium MRI, with a particular interest in the potential to link multi-quantum sodium MRI to underlying pathophysiological pathways<sup>6-9</sup>. In standard sodium imaging experiments, detection of the single-quantum (SQ) transition is performed directly after an excitation with similar approaches to conventional <sup>1</sup>H MRI. To exploit the potential of the spin 3/2 nuclei, multi-quantum coherence (MQC) signals are built by coherence transfer and combined over multiple acquisitions using radiofrequency phase cycling. Eventually, <sup>23</sup>Na triple-quantum coherences (TQC) might provide additional information related to cell vitality compared to the single-quantum coherences (SQC) signal alone<sup>10</sup>. A clear understanding of the mechanisms of MQC is necessary for relevant measurements and evading potential pitfalls. Currently, the description of MQC can be found in the clean form of the tensor formalism but spread in several manuscripts<sup>1,5,11-14</sup> dating of 15 years at the least. These highly theoretical descriptions neither offer an intuitive way of understanding multi-quantum mechanisms in the multidisciplinary field of MRI nor provide a basis to easily describe and relate the recent advances in triple-quantum (TQ) sodium NMR and MRI.

Sodium spin 3/2 nuclei exhibit four possible energy levels. Depending on the surrounding medium, different transitions between the levels are possible. The electric-quadrupole interaction determines the <sup>23</sup>Na relaxation processes and fundamentally distinguishes it from the dominant dipole-dipole interaction of proton nuclei. Due to the quadrupolar nature of the sodium nuclei, higher quantum coherences can be measured when the correlation time (describing the fluctuations of the electric field gradient, EFG, at the sodium nuclei)<sup>15</sup> exceeds the Larmor period. The EFG is generated by the electrons of the surrounding environment (i.e. proteins, lipids, macromolecules). In biologic environment, there is a fluctuating quadrupolar interaction, which adds to the Zeeman splitting and leads to a biexponential relaxation behavior so that MQC signals, in form of double quantum coherence (DQC) and TQC can be observed (Figure 1b). <sup>23</sup>Na MQC signal gives information about the interaction of the sodium nuclei with its surrounding environment in vivo. In an anisotropic environment, the quadrupolar moment of the sodium nuclei couples to the EFG which acts as relaxation mechanism leading to a more rapid decay of the outer than inner transitions of the spin 3/2 energy levels, resulting in a

biexponential T2 relaxation, with fast and slow components, which gives the possibility of MQC transfer due to violation of the coherence transfer rules<sup>1,4,16</sup>. In contrast, the quadrupole moment does not couple to an isotropic field, therefore no MQC can be measured in isotropic medium (e.g. saline solution).

A static quadrupolar interaction is observed in further macroscopically ordered environments, which is rare in biological medium but can be found in cartilage. DQC signal can yield information about the anisotropy in tissue because in ordered structures a preferred orientation of the quadrupolar sodium nuclei relative to the magnetic field B0 exists. DQC arise from two mechanisms: biexponential relaxation ( $T_{32}$ ) and quadrupolar splitting ( $T_{22}$ ), for specific information about the anisotropy a magic angle sequence selects the signal arising from  $T_{22}$ <sup>4,17,18</sup>. In contrast TQC signal arises only due to biexponential relaxation. Quadrupolar splitting within anisotropic structures has no additional effect<sup>11,12</sup>. Figure 1a shows the relevant processes<sup>16</sup>.

To measure and filter for different coherence pathways, in general, a three-pulses sequence is needed along with radiofrequency phase cycling to select the coherence of interest<sup>2</sup>. In the presented paper, we want to give an intuitive and pictorial understanding of phase cycling-based MQC build-up and the available choices in the corresponding three-pulses-experiment. The purpose was to seek optimal efficiency of a three-pulses sequence, defined in this scope as the minimum number of cycles and steps per cycle to provide a complete and unbiased measurement of MQC sodium signals. Thus, a time-efficient sequence design is drawn from analytical and simulation results. This sequence is guaranteed to withstand B0 and stimulated echo biases and is optimal for clinical MQC imaging methods. Experimental results demonstrate the potential of proposed Cartesian imaging of single and triple-quantum <sup>23</sup>Na (CRISTINA).

## THEORY

The pulse sequence is depicted along with the coherence pathway scheme in Figure 1. The conventional three-pulses experiment introduces three time-constants as parameters that impact the eventual measured signal. Among these three,  $\tau_2$  is usually minimized to neglect relaxation between the second and the third pulse, but the evolution time,  $\tau_1$ , and the echo time, TE, are in strong relation with the biexponential relaxation that separates SQC from DQC and TQC. The sequence is repeated while cycling the phases of the RF pulses. The first pulse-phase,  $\phi_1$ , cycles through a defined phase cycle while the second pulse is phase-shifted by the “phaseshift,  $\xi$ ” relative to the first pulse. The second pulse phase  $\phi_2$  will be given in relation to the first throughout the paper by its phase shift  $\xi = \phi_2 - \phi_1$ . The phase of the third pulse is set to  $0^\circ$ , as is the receiver phase. Exploiting the differences in evolution frequency between the MQC signals, an addition of the signals leads to constructive and destructive interference of the MQC pathways depending on the selected phase cycling scheme. The multiple aspects of MQC measurements are covered in the following.

Different phase cycling options have been proposed to eliminate potential biases in MQC measurements. Four options have been highlighted, which are presented in summary in Table 1:

First, the original 6 steps phase cycle, option I, which samples the coherence evolution over a  $2\pi$  interval with a phase increment of  $\pi/3$ , a phase shift  $\xi = \pi/2$ ,  $\phi_{1,t=0} = \pi/6$  and a constant phase for the third pulse and the receiver of  $0^\circ$ <sup>1</sup>. The phase increment of  $\pi/3$  places the TQ frequency at the Nyquist limit.

Second, option II, the 2x8-steps NMR method of triple-quantum (time) proportional phase increments (TQTPPI). This NMR method was developed to alleviate the need to optimize,  $\tau_1$  and TE, but rather to capture the relaxation constants,  $T2^*$ slow and  $T2^*$ fast by incrementing  $\tau_1$ .<sup>19</sup> This sequence was employed for sodium TQC measurement with an 8-step phase cycling, proposed to measure directly the T2 relaxation<sup>20</sup>. Its advantage is a signal acquisition free of assumptions on the sample(s) relaxation parameters. The TQ(T)PPI with optional increments of the evolution time was used by<sup>1,20</sup> with a phase shift of  $\xi = +\pi/2$ . An additional 8-step phase cycle with  $\xi = -\pi/2$  was proposed to eliminate DQC with  $\phi_{1^{1st\_cycle}} = \phi_{1^{2nd\_cycle}}$ .



Third, option III, a 2x6-steps cycle for recovering signal cancellation due to deleterious effects of B0 inhomogeneity was proposed by Fleysher et al. 2010<sup>21</sup>. In MRI, B0 inhomogeneity can be severe and lead to spins dephasing and MQC signal loss. An additional 6 step phase cycle was introduced with phase shift  $\xi = 0$  (Table 1). Gradient spoiling during evolution time would be an alternative to mitigate B0 inhomogeneity impact but lowers the SNR due to the spoiling of half the coherence pathway contributions.

Fourth, option IV, uses 4x6 steps phase cycling to avoid bias due to T1-weighted stimulated echo signals, presented by<sup>22</sup>. Signal bias can arise due to stimulated echo (STE) signal for which a solution, the SISTINA sequence, was proposed by Tanase et al. 2005 and Fiege et al. 2013<sup>13,22</sup>. In general, a three-pulses sequence can form a STE signal<sup>23-25</sup> that could give an unwanted bias. An additional phase cycle was introduced with a phase shift of  $\xi = -\frac{\pi}{2}$ . SISTINA chose two 6-steps phase cycles, with phase shifts  $\xi = \pm \pi/2$ , to eliminate STE signal. B0 inhomogeneity was compensated for with two extra phase cycles, using the same approach as in option III.

In the following, the impact of STE versus B0 offset was investigated to make a founded choice, our option V, for optimal MQC measurement.

## METHODS

### SIMULATION

For the formulation of the signal equations, <sup>21</sup> formalism was chosen and detailed description can be found ([https://github.com/MHoesl/MQC\\_Simulation](https://github.com/MHoesl/MQC_Simulation)). The coherence levels after the first and second RF pulses are denoted by p1 and p2 respectively. The matrix  $A_{p1,p2}$  was specified as the amplitude of the respective coherence pathway:

$$A_{p1,p2} = \begin{array}{c|cccccc} \begin{array}{c} p2 \rightarrow \\ p1 \downarrow \\ -1 \\ +1 \end{array} & \begin{array}{c} -3 \\ -2 \\ -1 \\ +1 \\ +2 \\ +3 \end{array} & & & & & \\ \hline & -TQ/4 & -DQ/4 & -SQ/4 & -SQ/4 & -DQ/4 & -TQ/4 \\ & TQ/4 & DQ/4 & SQ/4 & SQ/4 & DQ/4 & TQ/4 \end{array}$$

An initial amplitude set (SQ, DQ, TQ) for the coherence level transfers is thus divided into its multiple possible pathways. For example, there are four possibilities for the TQC (drawn in green in Figure 1c). One of these four pathways starts from the coherence level p1=-1 after the first pulse. The second pulse transfers to the coherence level to p2=-3, resulting in the signal from T<sub>3-3</sub>. The received signal, S, cumulates all coherence pathways and is expressed as:

$$S(\tau_1, \tau_2, \phi_1, \phi_2, \Omega, TE) = \sum_{p1} \sum_{p2} e^{-i(p1\phi_1 + (p2-p1)\phi_2)} B_{Na}(p1, p2, \tau_1, \tau_2, \Omega, TE, A_{p1,p2}) \quad [1.1]$$

$$B_{Na} = e^{-i(p1\tau_1 + p2\tau_2)\Omega} e^{i\Omega TE} A_{p1,p2}$$

The parameter  $\Omega$  (Hz) in the term  $B_{Na}$  describes the off resonances effects, for simulation of magnetic field inhomogeneity. Theoretically, the signal S is nulled for:

$$S(\Omega) = 0 \text{ for } \Omega(\text{Hz}) = \frac{k\pi + \xi 1}{2\pi\tau_1}, k \in \mathbb{N}_0$$

Details of this calculation can be found in supplementary materials S.4. For the first simulation part, relaxation terms were omitted. For the second simulation part, the following equations were formulated to take into account relaxation effects within the amplitude matrix  $A_{p1,p2}$ . Transverse relaxation for the SQ signal was described by the biexponential decay separated into T2\*slow and T2\*fast components and the excitation angle  $\theta_{exc}$ :

$$SQ = SQ_0 \left( \frac{3}{5} e^{-\frac{(TE+\tau_1)}{T2^*_{slow}}} + \frac{2}{5} e^{-\frac{(TE+\tau_1)}{T2^*_{fast}}} \right) \sin(\theta_{exc}) \quad [1.2]$$

For the DQ and TQ coherence signals, the relaxation terms are given by:

$$MQ = MQ_0 \left( e^{-\frac{TE}{T2^*_{slow}}} - e^{-\frac{TE}{T2^*_{fast}}} \right) \left( e^{-\frac{\tau_1}{T2^*_{slow}}} - e^{-\frac{\tau_1}{T2^*_{fast}}} \right) e^{-\frac{\tau_2}{T2^*_{slow}}} \sin^5(\theta_{exc}), \text{ with } MQ = DQ, TQ \quad [1.3]$$

The stimulated echo (STE) signal depends on the flip angle (or B1+), relaxation effects and B0 inhomogeneity and was described as follows:

$$S_{STE} = \sum_{p_1} \sum_{p_2} e^{-i(p_1(m)\phi_1 + (0-p_1(m))\phi_2)} B_{STE}(\tau_1, \tau_2, \Omega, TE, \xi, T_1, T2^*_{slow}, T2^*_{fast}, A_{p_1, p_2}) \quad [1.4]$$

$$B_{STE} = \frac{|A_{p_1, p_2}|}{2} e^{-\frac{\tau_2}{T_1}} \cos(\xi - \Omega\tau_1) e^{i\Omega TE} \left( \frac{3}{5} e^{-\frac{(TE-\tau_1)^2}{2T2^*_{slow}}} + \frac{2}{5} e^{-\frac{(TE-\tau_1)^2}{2T2^*_{fast}}} \right) \quad [1.5]$$

The maximum of  $B_{STE}$ , with respect to the echo time, is found for  $TE = \tau_1$ . We used the following parameter values, in accordance with realistic measurement values:  $\tau_1=10$  ms,  $\tau_2 = 100 \mu\text{s}$ ,  $T2^*_{slow} = 30$  ms,  $T2^*_{fast} = 4$  ms,  $T1 = 70$  ms. All three flip-angles were set to  $\pi/2$ . The MQC signal contributions, which populate the matrix  $A_{p_1, p_2}$ , were set to 1.0, 0.5 and 0.3 for the SQ, DQ and TQ coherences respectively to ease visualization. Assuming sufficiently long TR values ( $>120$  ms), notably to fit practical SAR limitations in MRI, longitudinal relaxation was further neglected in the simulations.

**SIGNAL RECONSTRUCTION:** MQC signals can be separated by their scaled evolution frequencies, as defined by their phase term  $\exp(-i(p_1\phi_1 + (p_2 - p_1)\phi_2)) = \exp(-ip_2\phi_1) \exp(i(p_2 - p_1)\xi)$ . The spectrum signal is thus reconstructed by Fourier Transformation (FT) along the phase dimension  $\phi_1$ . According to Fleysher, the signals,  $S$ , of the two phase-cycles, are transformed independently:

$$\hat{S}_{\{\xi\}} = FT(S_{\{\xi\}}), \quad \xi = \frac{\pi}{2}, 0 \quad [2.1]$$

$\hat{S}$  denotes the spectrum, normalized to the size of the signal to obtain correct FT amplitude values. The two spectra are combined to  $\hat{S}_{\pm}$ .

$$\hat{S}_{\pm} = \frac{1}{2} \left( \hat{S}_{\{\xi=0\}} \pm i \hat{S}_{\{\xi=\frac{\pi}{2}\}} \right) \quad [2.2]$$

A fully recovered spectrum,  $\hat{S}$ , can be calculated if the B0 offset,  $\Omega$ , is known. Signal dephasing occurs during the evolution time and the echo time, and the signal can be recovered with its phase:

$$\hat{S}_{reco}|_{t=TE, B0 \text{ offset}=\Omega} = \frac{1}{2} \left( \hat{S}_+|_{TE, \Omega} e^{+i\Omega\tau_1} - \hat{S}_-|_{TE, \Omega} e^{-i\Omega\tau_1} \right) e^{-i\Omega TE} \quad [2.3]$$

For the SISTINA reconstruction, in total four cycle-signals (4x6 steps) were proposed to offer a full reconstruction correcting for STE signal and B0 offset (Figure 3). But in

vivo SISTINA acquisitions were limited to phase cycles 1 and 2 only. Thus, the reconstruction was reported as individual signal FT and sum-of-squares combination:

$$\hat{S}_{\{n\}} = FT(S_{\{n\}}) , n = 1,2,3,4 , \quad \hat{S}|_{in vivo} = \sqrt{\hat{S}_1^2 + \hat{S}_2^2} \quad [2.4]$$

$$\hat{S}|_{total} = \sqrt{\hat{S}_1^2 + \hat{S}_3^2 + \hat{S}_2^2 + \hat{S}_4^2} \quad [2.5]$$

The signals,  $S$ , and resulting spectra,  $\hat{S}$ , were simulated for I) the original 6-step phase cycle as well as the highlighted options II) 2x 8-step TQ(T)PPI phase cycle III) the 2x6 step phase cycles of Fleysher and IV) the 4x6 phase cycles of the SISTINA sequence.

#### EXPERIMENTAL ACQUISITIONS

To complement the simulation work, measurements on two phantoms and in the brain of five healthy volunteers were performed. Experiments were performed on 7T MRI (Siemens Magnetom, Erlangen, Germany) with a 1Tx/1Rx dual-tuned  $^1\text{H}/^{23}\text{Na}$  head coil (QED, Cleveland, USA). One phantom was a simple bottle of saline water. The second phantom consisted of 8x60 ml tubes with varying concentrations of agarose (0%-5%) and sodium (50-154 mM). The study was approved by local ethical committee and volunteers were recruited after providing informed consent according to the Declaration of Helsinki. Three vials were placed next to the head, with concentrations of agarose and sodium of: [4% 100mM], [4% 50mM] and [2% 100mM] to allow subsequent calculations of TSC and comparison of TQ signal. A multi echo Cartesian MQC imaging sequence was developed that features the possibility of easy switching between different phase cycle choices by variable  $\Phi_0$ ,  $\Delta\Phi$  and phase shift  $\xi$ . A Cartesian readout was chosen for efficiency and ease of reconstruction, as well as the fact that the TQC signal of interest is maximal at a later echo time (Figure 1b). Efficiency considerations included the number of measured points per phase cycle and the use of a multi-echo readout which allows signal capture of both TQC (later echo times) and SQC (early echo times) as well as the possibility of reconstructing a  $B_0$  map directly from the data.  $\Delta\Phi$  was conservatively chosen to be  $30^\circ$  which results in a 2-fold oversampling of the TQC frequency. The 12-steps phase cycle of  $2\pi$  was averaged over 10 repetitions in phantom and 12 repetitions in vivo. Other parameters

were: 32x32 matrix size with 2-fold oversampling in readout direction, FOV of 200mm (phantom) and 250 mm (in vivo), bandwidth of 330Hz/Px and the 2D slice thickness was 20mm. CRISTINA phase cycles were chosen identical to option III based on the simulation results for acquisition of B0-unbiased TQ signal. The multi-echo readout included 20 TEs, with  $TE_1 = 1.15$  ms (asymmetric echo) and  $\Delta TE = 3$  ms. The TR was 390 ms due to SAR restrictions and acquisition time was 25 min (phantom) and 29 min (in vivo) per cycle, which corresponds to 50 min and 58 min total acquisition time respectively. The optimal evolution time  $\tau_1$  was determined experimentally from a TQTPPI global spectroscopic pre-scan (scan time 1-2 min) and a subsequent offline fit. Thus employed  $\tau_1$  values were: 10 ms in the first phantom (no optimization for pure saline water), 13 ms for the second phantom and  $9.2 \pm 1.4$  ms for in vivo brain. In the saline water bottle, a 1D strong static magnetic gradient was applied ( $\sim 10$ Hz/1cm) to induce off-resonance artifact. CRISTINA was compared to its counterpart SISTINA with in-vivo phase cycles (REF: Fiege13 and Worthoff14) as defined in Table 1. Since SISTINA uses 6-step phase cycles, the number of averages was set to 20 to match CRISTINA total acquisition time.

#### *EXPERIMENTAL DATA ANALYSIS*

The first two echoes from CRISTINA phase data served to map sodium signal off-resonance (B0). Combining CRISTINA two phase cycles ( $\xi_1 = \pi/2$  and  $\xi_2 = 0$ ), a voxel-wise multiparametric fit of  $^{23}\text{Na}$  signal parameters was performed, providing maps of  $T2^*$ slow and  $T2^*$ fast using Equations [1.2] and [1.3] and including a DC component to account for background noise. The minimum of the multivariable function was approached with GlobalSearch and fmincon solver in Matlab. The value of TQC at  $TE = 0$ ms is zero from theory and was added to the multi-echo data to enhance the fit. The SQC signal at  $TE = 0$  ms was obtained by extrapolation of the fit result, thus enabling an estimate of a zero-TE sodium signal. The fit function included both  $T2^*$ fast and  $T2^*$ long compartments. The fit's lower boundary of the  $T2^*$ fast component amplitude was set to 0 to enable the finding of a 'mono-exponential' solution. Thus, both bi-exponential and mono-exponential solutions could arise. In the second phantom, the fitted values were evaluated in circular regions of interest centered over each of the eight phantom tubes independently, avoiding partial volume effect. Tissue sodium concentration to signal relationship was evaluated in the ROI

for the SQC image at TE = 0ms. TQC image at TE =  $\tau_1$ , normalized by SQC image at TE = 0 ms was plotted against agar percentage and provided TQ/SQ ratio.

Finally, SNR was measured in separated TQ and SQ images over multiple TE. SNR was defined as mean signal averaged over the body mask divided by the standard deviation of signal in the air. In vitro SNR was averaged over all phantoms and in vivo SNR was measured over the entire brain.

## RESULTS

### *SIMULATION*

The simulation of the original 6-steps phase cycle with neither B0 inhomogeneity,  $\Omega$ , nor relaxation effects, Option I, is presented as Supporting Information Figure S1, for completeness. The choices for the 6 samples appear relevant to measure the full amplitude of the TQC signal, whereas DQ is not optimally sampled. Also, the choice for 6 samples places the TQC signal at the Nyquist limit. Fourier Transformation along the evolution phase  $\phi_1$  recovers the amplitudes of the mixed signal of (SQ, DQ, TQ) = (1.0, 0.5, 0.3). The amplitudes in the spectrum do not have a Lorentzian shape because the phase cycle does not capture relaxation processes.

Second, regardless of the time-increments (therefore the name TQ(T)PPI), the TQPPI samplings for the two phase-cycles with  $\xi = \pm \pi/2$  are depicted in Figure 2, Option II. It is demonstrated that the phase increment choice, of  $45^\circ$ , oversamples the TQC signal. Specifically, the  $45^\circ$  phase increment samples the maximum of the TQ signal only in 2 out of 8 points, with 4 points falling short of measuring the maximum point. In contrast, the sampling points measure optimally the maximum amplitude of the DQC signal, which is opposite in signal for the two cycles and hence cancels out when the signals are combined. Without considering B0 offset, the SQC and TQC signal is equivalent for the two cycles with the signal ending up only in the imaginary channel. When relaxation processes and B0 offsets (100 Hz range) are included (Figure 4), an oscillatory pattern for all quantum coherences was observed with occurrences of complete signal loss. Signal cancellation can be observed for the two phase-cycle signals S1, S2 and the reconstructed spectra  $\hat{S}$  at the same frequency offset (25 Hz and 75 Hz). The signal dropouts can be obtained from

Eq.[1.1] for  $\Omega = (k\pi + \pi/2)/2\pi\tau_1 = (2k+1)/4\tau_1$ ,  $k \in \mathbb{N}_0$ , which corresponds to the measured dropout values. Further, it can be observed that the DQC signal suppression is also achieved when relaxation processes are considered, and a B0 offset alters the signal. Whereas the MQC magnitude signal is equivalent for the two cycles, the phase images show opposite signs for the DQC signal.

The third phase cycling, option III, dubbed here Fleysher's <sup>21</sup>, recognized the dramatic signal loss due to B0 inhomogeneity. The benefit of Fleysher's two cycles along with its reconstruction is explained in Figure 3, Option III, for an exemplary offset of 10 Hz. The full recovery of the signal (neglecting relaxation) can be seen directly in the amplitude values of the spectrum  $\hat{S}_{\text{reco}}$ .

The full simulation, including relaxation and a range of 100 Hz offsets shows again an oscillatory pattern for the MQC signals along the B0 offset with occurrences of complete signal loss (Figure 5). The key point is that the two cycles are complementary in exhibiting signal cancellation and signal maximum. The signal dropouts of the second cycle,  $\xi=0$ , are obtained for  $\Omega = (k\pi+0)/2\pi\tau_1 = k/2\tau_1$ . For our set of simulation parameters e.g. at an offset of  $\Omega = 25$  Hz the signal is recovered in the second phase cycle while being completely cancelled in the original phase cycle. The oscillation of the original signal thus has a counterpart in the additional phase cycle.

The simulation results for option IV, with phase cycles for stimulated echo (STE) mitigation can be found in Supplementary Material Figure S.3. The STE signal can overlap with MQC signals, which can be seen in Figure S.3.a and shows a relative maximum signal of 0.16 (red cross) at an echo time of  $TE = \tau_1 = 10$  ms which coincides with the maximum signal of the TQC signal (Figure 5). The STE phase signal is opposite for the phase cycles that were proposed by SISTINA and thus the sum of the complex STE signals of the two cycles cancels out.

However, considering STE signal expression, one can observe that STE is independent of the phase increment  $\phi_1$  as its phase term is  $\exp(i(p_1\phi_1 + (0 - p_1)\phi_2)) = \exp(ip_1\xi)$ . Thus, STE signal can be considered as a "zero-quantum coherence" (ZQC) signal. Finally, inserting measured B0 offset into equation [1.5] of the STE signal can nullify STE signal within the reconstruction. The alternatively proposed sum of

squares magnitude reconstruction, as indicated in the SISTINA publication<sup>22</sup>, still showed the STE signal as an offset.

Figure 6 compares the complete signal recovery from 2 cycles, as defined in Fleysher and presently, to the signal from the 4 cycles defined in SISTINA (refer to Table 1). B0-induced signal nulling in  $\hat{S}1$  and  $\hat{S}2$  was compensated for using paired cycles  $\hat{S}3$  and  $\hat{S}4$ , as shown in the reconstructed combination  $\hat{S}1+\hat{S}3$  (Figure 6.b). However, SISTINA choice to prefer the first cycles S1 and S2 for all in vivo experiments remains sensitive to B0-induced signal loss.

In summary, it appears crucial to compensate for B0 offsets while STE is inherently isolated upon Fourier transform of the MQC signals, as is DQC. Thus, an efficient choice for MQC measurements is Fleysher's 2x6-steps phase cycles. But SISTINA's design offered an interesting addition by electing for a multi-echo times readout to sample MQC signals along time (alas in a larger raster time than TQTPPI). Therefore, the combined design of 2x6-steps phase cycles and a multi-echo Cartesian Single and Triple quantum Imaging of sodium (<sup>23</sup>NA) (i.e. CRISTINA) was implemented and investigated on phantoms and in vivo in the following.



## EXPERIMENTAL MEASUREMENTS

Experimental comparison of CRISTINA and SISTINA shown in Figure 6.c confirms SISTINA sensitivity to B0 when using only the 2 “in vivo” cycles whereas CRISTINA design allows for a B0-resilient reconstruction of SQC signal (and by extension TQC). The signal loss between CRISTINA and SISTINA oscillates between 20 and 50 % due to intra-voxel signal averaging within large acquired voxels.

Figure 7 shows experimental design, including the CRISTINA sequence diagram (a), raw images (b), and the postprocessing results (c) exemplary from one voxel as well as for the whole image. The estimated  $\tau_1$  from a TQTPPI global spectroscopic pre-scan (scan time  $\sim 30$ s) was 13.3 ms. Two series of 4D images were obtained with the dimensions being x, y, TE and  $\phi_1$ . The Fourier transform along the repeated ( $\times 10$ ) phase cycle dimension  $\phi_1$  over the complex signal images showed the MQC spectrum as anticipated from the simulations. Selecting single and triple quantum coherence frequencies, the SQ and TQ images were reconstructed. Subsequently,  $\hat{S} +$  and  $\hat{S} -$  were calculated. A B0 map was also computed using the phase difference (unwrapped) between the first two TE after quadrature combination of the two phase-cycles and averaging over phase cycle steps. Eventually, total SQC and TQC signal images were reconstructed for each TE. Data and processing results for a single voxel can be found in the Supporting information Figure S.2 with the intention to enhance comparability to the simulation results.

A subsequent multiparametric fit for the SQC and TQC signals (Eq.1.2, Eq.1.3) was performed voxel-wise along the echo time data, enhanced by the prior knowledge that TQC is zero at TE = 0ms. The results are presented in Figure 8. The SQC signal evolution fit over the multiple echo times allowed for extrapolation of the SQC signal to TE = 0 ms. The TQC signal image is shown for TE= $\tau_1$ = 13.3 ms. Exemplary, the signal evolution measurement data with the corresponding fit results are shown for the 8 center voxels of the phantom vials along TE, in range of 0 to 60ms, separately for the SQC and TQC signal (Figure 8.e,f). The characteristic signal evolution of SQC and TQC signals from the simulation was confirmed. Eventually, T2\*fast and T2\*slow maps were produced from the multiparameter fit with values in the range of 0-12ms for T2\*fast and 15-30 ms for T2\*slow. The liquid phantom vial followed essentially a mono-exponential decay for most pixels (Figure 8(d)). The 2% agar vial in the center

showed elevated T2\* fast values in the range of (11±2.7)ms and lower T2\*long values of (21.9±3.1)ms compared to the 4% and 5% agar phantoms with T2\* fast in the order of 5ms and T2\* long in the order of 27 ms.

Further, mean SQC signal, evaluated in ROI, in the SQC image at TE = 0ms showed a linear relationship against total sodium content (TSC) in mM ( $R^2=0.75$ , p-value = 0.0058) (Figure 7g). For the mean TQC signal, normalized by SQC at TE=0ms, a higher signal strength was observed for increased agar content, regardless of the sodium concentration ( $R^2 = 0.87$ , p-value = 0.0007). However, for the 4% and 5% agar content, the mean TQC/SQC difference was within the ROI standard deviations.

Feasibility of in vivo CRISTINA is demonstrated in Figure 9. CRISTINA shows excellent resilience to B0 inhomogeneity, such as in the first volunteer in which B0-shimming was not iterated. SQ images at TE=1.15ms exhibit expected sodium distribution in the brain, despite significant partial volume effect of cerebrospinal fluid due the thick prescribed 2D slice (20mm). When comparing SNR between in vivo and in vitro (refer to Supplementary Material Figure S.5), it appears in vivo SQ SNR are equivalent: XX+- yy at TE=1.15 ms in vitro and ZZ +- WW at TE=9.7ms in vivo. However, maximum TQ SNR was insufficient in vivo (AA +- BB at TE=1.15ms) compared to phantoms SNR (CC +- DD at TE=9.7ms). Therefore, in vivo data were considered unsuited for reliable multiparametric fitting with the current methods.

## DISCUSSION

In this study, the rationales for the various sequence designs for multiple-quantum coherence sodium-MRI measurement were considered in a unified formalism, theoretically and graphically. From the improved understanding of the different options, an efficient design was proposed to compensate for  $B_0$  and stimulated echo in only 2x6-steps phase cycles. The proposed CRISTINA sequence further leveraged multi-echo readout to rapidly sample MQC signal temporal evolution. Eventually, CRISTINA data were enhanced by the unified formalism to draw a complete characterization of the sodium signal, including  $B_0$ , relaxometry, and total signal of both SQC and TQC.

Although different options have been presented over the last decades, an overview and comparison between the various techniques was lacking. Furthermore, we presented a graphical and intuitive formalism to simulate the techniques of coherence transfer and phase cycling, with publicly available code for reproducibility.

The understanding of the different options for measuring TQC signal along with the resulting efficient phase-cycling choice is especially important, as sodium MR techniques are on the rise thanks to hardware improvements. Eventually, probing MQC signal in sodium MRI allows to fully capture the underlying physical properties within each voxel. Indeed, as shown in Figure 8, both  $T_2^*$  compartments relaxation properties and total sodium concentrations can be inferred, provided that a calibrated sample is within the imaging plane. Thus, the pairing of the common theoretical framework presented above with the experimental design for efficient MQC sodium MRI can provide refined tissue characterization and hence diagnostics and treatment monitoring.

Simulation results showed that the conventional six step phase cycle is, expectedly, most susceptible to  $B_0$  inhomogeneity. The additional phase cycle with a phaseshift of  $0^\circ$  for  $B_0$  inhomogeneity mitigation effectively alleviates the problem.

The TQTPPI method proposed a different second phase cycle to suppress DQC signals. However, the DQC signal is differentiated by Fourier decomposition and ends up at twice the single quantum coherence frequency, whereas the TQC signal ends up at three times the SQC frequency. Therefore, the additional cycle for DQC transfer suppression doubles the measurement time with merely an averaging repetition of the SQC and TQC signal. The  $45^\circ$  ( $2\pi/8$ ) phase increment oversamples TQC and misses to capture the full TQC signal amplitude. The Nyquist sampling

frequency is twice the highest frequency of interest, resulting in a maximum phase increment of  $60^\circ$  for efficient TQC sampling. Any smaller phase increment results in oversampling and serves to accumulate signal, which can be substituted by averaging. The advantage of the TQTPPI method using time proportional phase increments is given in the possibility of obtaining the  $T2^*$  long and short values from the fit of the signal along the evolution time without prior knowledge of the optimal evolution time. A standard phase-cycle with fixed evolution time  $\tau_1$  and one single echo readout in an imaging experiment cannot provide this information. The Fleysher's two phase cycles choice focused on the  $B0$  offset mitigation. This design effectively helps to resolve any lost signal and remove STE and DQC signals impact while operating at the Nyquist frequency.

The SISTINA design focused on four phase cycles to suppress stimulated echo signals. Although the stimulated echo signal is the highest at the time point of the maximum TQC signal, the stimulated echo signal assimilates to a ZQC signal, i.e. as a continuous offset, after Fourier decomposition. SISTINA interesting aspect was the multiple echo readout that allows to capture the temporal evolution of both SQC and TQC. A further addition of the SISTINA sequence<sup>22,26</sup> was the use of the 'dead' time between the first and the second pulse for one or multiple UTE readouts. These additional measurements can serve to improve the overall SNR but combining UTE and further Cartesian images with proper signal scaling is non-trivial. Our CRISTINA results also demonstrate complete SQC signal characterization without UTE sampling.

Eventually, CRISTINA added values over SISTINA are multiple and arise from the proposed theoretical framework that was incomplete in the SISTINA design:

First, SISTINA considered 4 cycles to be necessary to complete sodium signal characterization. As demonstrated in Figure 6, CRISTINA two cycles suffice to compensate  $B0$ -induced signal loss and phase cycling inherently separates STE from MQC signals. Thus, in-vivo SISTINA results have been limited to  $B0$  homogeneity under  $(2k+1)/(4 \times 7\text{ms}) = 35\text{ Hz}$ ,  $107\text{ Hz}$  etc. (Worthoff et al. 2019) and  $(2k+1)/(4 \times 6\text{ms}) = 42\text{ Hz}$ ,  $125\text{ Hz}$  etc. (Fiege et al. 2013). Third, CRISTINA builds on an assumption-free signal model that allows proper sodium signal characterization. Proposed SISTINA signal model in Worthoff et al (Worthoff et al. 2019) used two erroneous

assumptions: a fixed ratio of 60/40 % of fast and slow decaying signal and a separation of intra and extra cellular signals based on relaxation properties alone <sup>27</sup>. CRISTINA model estimates all accessible parameters without a priori information. Fourth, CRISTINA relies only on Cartesian sampling whereas SISTINA is based on a joint model including half-radial UTE signal sampling and Cartesian sampling. UTE sampling is dedicated to measure rapidly decaying signal but suffers from accrued sensitivity to hardware imperfections (TylerJMRI07) that usually requires platform-dependent tuning and corrections. Utilizing Cartesian sampling only facilitates reproducibility across platforms and avoids the issue of scaling UTE and MQC Cartesian signals to jointly model signal relaxation.

Finally, CRISTINA additionally provides a B0 map that can serve the model from Eq.[2.3]. If B0 values were unavailable, a quadrature combination of the two cycle can be substituted, alas without exact signal phase.

Thus, an efficient MQC sodium-MRI sequence design – named CRISTINA - was drawn that benefits from the efficient Fleysher's 2x6-steps phase cycles, in combination with SISTINA multi-echo readout to mimic TQTPPI assumption-free signal sampling. CRISTINA leads to a complete characterization of sodium signal, including B0, relaxation times and MQC signals relative amplitudes.

#### *EXPERIMENTAL PROOF OF CONCEPT*

CRISTINA design was empowered by the theoretical formalism to extract MQC signals free of B0, DQC and STE biases. The reconstruction of the acquired Cartesian MQC data can be done straightforward using Fourier transform. B0 can be mapped using a simple least-square fit of the phase data. And a multiparametric fit results in T2\*fast and T2\*slow maps as well as quantification values for SQC and TQC signals. The asymmetric echo choice reduced the lowest possible TE to 1.15 ms and with extrapolation of the fit a TE = 0ms SQC image can be reconstructed, which allows TSC quantification without bias due to differing decay rates. Therefore, all relevant information for quantification methods can be obtained with the sequence.

Further optimization remains to be considered regarding acquisition parameters such as TE sampling, receiver bandwidth. Currently, the phantom measurement took 25 min per phase cycle but was chosen with conservative values of 2-fold oversampling the TQ frequency by  $\Delta\text{Phi} = 30^\circ$  and measurement of 10 full phase cycles for averaging. The total measurement time of 50min could, therefore, be reduced by  $\Delta\text{Phi} = 60^\circ$  and fewer phase cycles. The matrix size of 48x32 was chosen, and the higher resolution was achieved by zero filling. In vivo measurements were successfully conducted with the same parameters. Twelve full cycles were acquired, which resulted in an acquisition time of 29 min per cycle. Further tests in vivo are necessary to reduce the measurement time and for higher resolution scans without sacrificing SNR in the TQ image. Postprocessing of the cycle repetitions and the multiparametric fit could be optimized in the future by e.g., using a neural network approach<sup>28,29</sup>, and even considering the multiple dimensions instead of working voxel per voxel. Moreover, it must be noted that at present, CRISTINA remains a 2D imaging sequence, and for the presented measurement set a relatively thick slice of 20mm was used.

(phantom measurement raw data and reconstruction code can be found here: [https://github.com/MHoesl/MQC\\_Imaging\\_CRISTINA](https://github.com/MHoesl/MQC_Imaging_CRISTINA))

**In conclusion**, we presented a full simulation analysis of the different possible phase cycles for sodium multi-quantum MRI and highlighted their benefits and shortcomings. An efficient design was drawn, resulting design from the simulation work, and implemented on a clinical MRI. An experimental proof-of-concept on a phantom showed promising results for a complete characterization of the multi-quantum sodium signals.

## LIST OF FIGURE CAPTIONS

**Figure 1:** (a) ( $^{23}\text{Na}$ ) spin 3/2 nuclei interaction with a magnetic field: In isotropic environment, the ground state splits into the 4 different energy levels with equidistant levels. In biologic environment fluctuating quadrupolar interaction leads to the observation of DQC and TQC. Static quadrupolar interaction in ordered environments is rare in biological medium.

(b) the three pulses experiment used to achieve multi quantum coherence (MQC) transfer (c) coherence transfer diagram for pathways that can be probed. Relaxation between the first and second pulse,  $\tau_1$ , is crucial for TQC creation. The time between the second and third pulse ( $\tau_2$ ) is chosen as short as possible to limit MQC signal loss. The tensor  $T_{\text{rank,order}}$  changes its order after each RF pulse whereas only relaxation and quadrupolar coupling change the rank of the tensor. In perfect quadrature detection, only coherence level of -1 is observable. However, imperfect quadrature detection is common in MRI and signals can end up in the +1 pathway as well.

**Figure 2: Option II:** TQ(T)PPI phase cycling. The SQC and DQC are optimally sampled however the TQC maximum is only sampled at 2 out of 8 points. Evolution time increment and relaxation have been discarded. The sum of the two cycles signals effectively cancels out DQC signal. In the resulting spectra the DQC cancellation can be observed, and oversampling leads to TQC being split in 2 components.

**Figure 3: Option III:** Fleysher cycles for recovering B0 offset bias. Their addition and subtraction  $\hat{S}_+ \hat{S}_-$ , in combination with a reverse of the known B0 offset, results in the recovered spectrum (e). The amplitudes in e) are the initially set values for the simulation which shows that the signal was effectively recovered, independently of the B0 offset.

**Figure 4:** Option II TQ(T)PPI simulation including relaxation and B0 offset. The magnitude and phase of the signals at  $\phi_0$  are shown independently for the three quantum coherences, (a)SQC, (b)DQC and (c)TQC. The complex DQC signal (Row II.) shows signal cancellation due to opposite phases for the two phase-cycles. For the SQC and TQC signals, signal addition is constructive. (d) and (e) show the spectra for the individual phase cycles ( $\xi = \pm \frac{\pi}{2}$ ) as well as for the added signals in (d) along the B0 offset and (e) along the echo time. Signal cancellation at 25Hz and 75Hz can be observed.

**Figure 5:** Option III, Fleysher cycles, along echo time (0ms to 50ms) and varying B0 offset from 0Hz up to 100Hz: Magnitude and phase signal are shown for the SQC and TQC to show the differing oscillation due to B0 offset. This offers the possibility of signal reconstruction, shown in the spectra data in (c). Signal evolution with differing signal maxima of SQC and TQC signal along echo time is given for no B0 offset. Then the spectra are given at TE = 10ms along a B0 offset from 0 to 100Hz. Signal vanishing can be observed at 25 Hz and 75 Hz offset in the first cycle and at 0, 50 and 100 Hz in the second cycle. The reconstructed spectrum is independent of the B0 field offset.

**Figure 6: I:** SQC and Stimulated echo (SE) signal for varying echo time (TE) from 0ms to 30ms (x-axis) and varying B0 offset from 0 to 100Hz (y-axis). (a) SQ Signal without SE signal bias, (b) shows only the SE signal, with the expected maximum at 10ms which coincided with the set evolution time  $\tau_1$  (c) SQ signal with SE signal bias, for varying echo time (TE) from 0ms to 30ms (x-axis) and varying B0 offset from 0 to 100Hz (y-axis).

II: Option III phase cycle choice under STE and B0 offset bias: STE signal bias is visible at the zero-frequency position in Fourier domain, at echo time TE 10 ms and varies along B0 offset in the independent two cycles. B0 offset from 0 to 100Hz (y-axis). (e) Reconstruction using B0 values lead to full recovery with no STE offset. (f) The sum of squares reconstruction did not remove the STE offset. III: Option IV, SISTINA phase cycles simulated

with STE signal bias. On the right of the arrow the spectra were reconstructed from the data (a-d) (e) magnitude reconstruction of S1 and S2. (f) magnitude reconstruction of S1 and S3 (g) magnitude reconstruction of all four contributions. STE signal was not removed in the reconstructions and still visible in the zero frequency. (e) choosing the two first phase cycles keeps the B0 inhomogeneity bias.

**Figure 7:** (a) 2D multi-echo sequence scheme (b) initial phase cycle signal image at  $\Phi_{1,t=0}$  (d) from the phase cycle data, the spectroscopic images were reconstructed by voxel wise FT, for each TE set.  $\hat{S}^+$  and  $\hat{S}^-$  were calculated. The B0 map was calculated from quadrature combination of the two cycles and the multi TE experiment. Using the voxel wise B0 offset values, the total spectroscopic result,  $\hat{S}_{total}$ , was reconstructed. A complex signal depiction of a voxel of interest, in phantom 5 can be found in the supporting information Figure S.2.

**Figure 8:** (a) fitted SQ signal, extrapolated to TE = 0ms. The colorbars show the signal strength and the sodium concentration in mM by a linear fit using the (2%, 130mM and 100mM) phantoms for calibration. Phantoms are numbered for the following. (b) TQ signal at TE 13.3 ms with higher signal strength in phantoms 3 and 5 (4%, 5% agar, 154mM). (c) TQ to SQ ratio relates to agar values, independent of sodium content (d,e) T2\* slow and T2\*fast maps by voxel wise fit. The liquid phantom 1 showed a mono-exponential result and therefore has values close to zero. (f) TQ to SQ ratio is visualized against agar concentration and showed a linear relationship ( $R^2 = 0.87$ ). (g) SQ signal at TE = 0ms showed a linear relationship to sodium concentration ( $R^2 = 0.75$ ). Values in f,g were evaluated and averaged over the tube size. (h) SQ signal over echo time and fit, only four phantoms, different in agar and sodium concentration, are depicted to ease visual comparison. (i) TQ signal over echo time and fit. Table S.3 with T2 slow and T2 fast values, along with the concentrations of each of the numbered phantoms, can be found in the supporting information.

**Figure 9:** (a,b) T2w image and the 2D slice position for the sodium acquisition in coronal and axial view (c) initial phase cycle signal at  $\Phi_{1,t=0}$  for the first cycle (d) reconstructed SQ image for the first cycle. (e,f) TQ images for both cycles. (g) B0 map leading to the total spectroscopic signal,  $\hat{S}_{total}$ . To enhance SNR the TQ images are averaged from the 2<sup>nd</sup> to the 7<sup>th</sup> echo which equals the echo times from 4ms to 18ms.

**Table 2:** Overview over the highlighted phase-cycle options



## Supporting Information Figures:

**Figure S.1:** Option I: Original six step phase cycle: (a) the three coherence signals contributions over the evolution phase  $\phi_1$  dimension. Circle markers highlight sampling values for phase increment of  $2\pi/6$  and start phase of  $\pi/6$ . (b) Fourier Transform splits the MQC contributions and thus allows to separate the three contributions SQ, DQ and TQ, with TQ signal at the Nyquist horizon.

**Figure S.2:** For better comparison to the simulation data, a single voxel of interest within Phantom 5, 154 mM Na, 5% agar is presented. (a), (b) image data with the voxel of interest marked by a cross. (c) Real and Imaginary parts of the two cycles are plotted along  $\phi_1$  with the circular markers indicating data acquisition. (d,e) spectroscopic result along the multiple echo times. (d) TQ signal can be seen well (e) no visible TQ signal in (e). (f) The data are reconstructed to a total spectroscopic result free of B0 inhomogeneity bias.

**Table S.3:** mean phantom T2\* values, evaluated in a circular ROI of phantom diameter size. The four smaller diameter phantoms were not taken into account and served to see if smaller structures can be resolved.

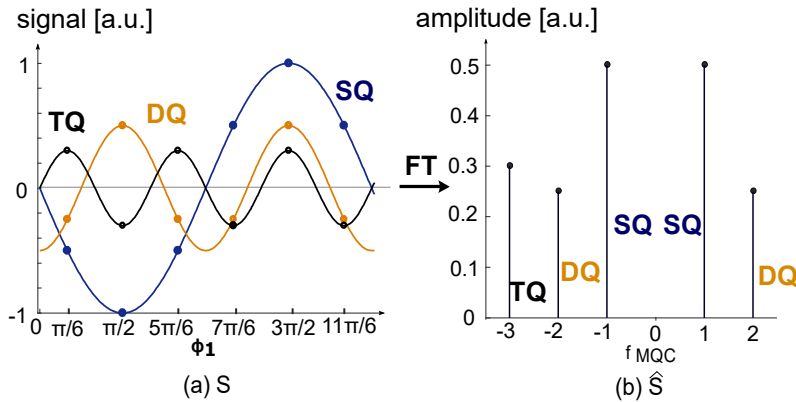
## REFERENCES

1. Jaccard G, Wimperis S, Bodenhausen G. Multiple-quantum NMR spectroscopy of  $S=3/2$  spins in isotropic phase: A new probe for multiexponential relaxation. *J Chem Phys*. 1986;85(11):6282. doi:10.1063/1.451458
2. Bodenhausen G, Kogler H, Ernst RR. Selection of coherence-transfer pathways in NMR pulse experiments. *J Magn Reson*. 1984;58(3):370-388. doi:10.1016/0022-2364(84)90142-2
3. Bodenhausen G, Vold RL, Vold RR. Multiple quantum spin-echo spectroscopy. *J Magn Reson*. 1980;37(1):93-106. doi:10.1016/0022-2364(80)90096-7
4. Pekar J, Leigh JS. Detection of biexponential relaxation in sodium-23 facilitated by double-quantum filtering. *J Magn Reson*. 1986;69(3):582-584. doi:10.1016/0022-2364(86)90180-0
5. van der Maarel JRC. Relaxation of spin quantum number  $S=3/2$  under multiple-pulse quadrupolar echoes. *J Chem Phys*. 1991;94(7):4765. doi:10.1063/1.460561
6. Romanzetti S, Mirkes CC, Fiege DP, Celik A, Felder J, Shah NJ. Mapping tissue sodium concentration in the human brain: A comparison of MR sequences at 9.4 Tesla. *Neuroimage*. 2014;96:44-53. doi:10.1016/j.neuroimage.2014.03.079
7. Thulborn KR. Quantitative sodium MR imaging: A review of its evolving role in medicine. *Neuroimage*. 2018. doi:10.1016/j.neuroimage.2016.11.056
8. Wagner D, Anton M, Vorwerk H. Dose uncertainty in radiotherapy of patients with head and neck cancer measured by in vivo ESR/alanine dosimetry using a mouthpiece. *Phys Med Biol*. 2011;56(5):1373-1383. doi:10.1088/0031-9155/56/5/010
9. Hu R, Kleimaier D, Malzacher M, Hoesl MAU, Paschke NK, Schad LR. X-nuclei imaging: Current state, technical challenges, and future directions. *J Magn Reson Imaging*. 2019;0(0). doi:10.1002/jmri.26780
10. Hoesl MAU, Kleimaier D, Hu R, et al.  $^{23}\text{Na}$  Triple-quantum signal of in vitro human liver cells, liposomes, and nanoparticles: Cell viability assessment vs. separation of intra- and extracellular signal. *J Magn Reson Imaging*. 2019:1-10. doi:10.1002/jmri.26666
11. Van Der Maarel JRC. Thermal relaxation and coherence dynamics of spin  $3/2$ . I. Static and fluctuating quadrupolar interactions in the multipole basis. *Concepts Magn Reson Part A Bridg Educ Res*. 2003;19(2):97-116. doi:10.1002/cmr.a.10087
12. Van Der Maarel JRC. Thermal relaxation and coherence dynamics of spin  $3/2$ . II. Strong radio-frequency field. *Concepts Magn Reson Part A Bridg Educ Res*. 2003;19(2):117-133. doi:10.1002/cmr.a.10088
13. Tanase C, Boada FE. Triple-quantum-filtered imaging of sodium in presence

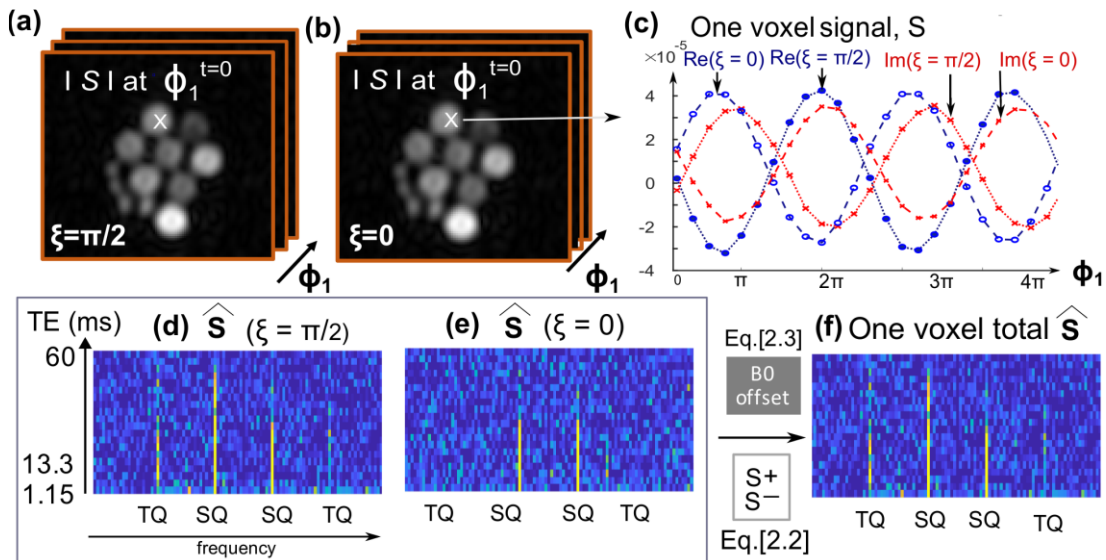
- of B<sub>0</sub> inhomogeneities. *J Magn Reson*. 2005;174:270-278.  
doi:10.1016/j.jmr.2005.02.012
14. Schepkin VD. Statistical tensor analysis of the MQ MR signals generated by weak quadrupole interactions. *Z Med Phys*. 2019;29:326-336.  
doi:10.1016/j.zemedi.2019.03.002
  15. Levitt MH. *Malcolm H. Levitt.*; 2000.
  16. Rooney WD, Springer CS. The molecular environment of intracellular sodium: <sup>23</sup>Na NMR relaxation. *NMR Biomed*. 1991;4(5):227-245.  
doi:10.1002/nbm.1940040503
  17. Kemp-Harper R, Brown SP, Hughes CE, Styles P, Wimperis S. <sup>23</sup> Na NMR methods for selective observation of sodium ions in ordered environments. *Prog Nucl Magn Reson Spectrosc*. 1997;30(3-4):157.
  18. Navon G, Shinar H, Eliav U, Seo Y. Multiquantum filters and order in tissues. *NMR Biomed*. 2001;14(2):112-132. doi:10.1002/nbm.687
  19. Marion D, Wüthrich K. Application of phase sensitive two-dimensional correlated spectroscopy (COSY) for measurements of <sup>1</sup> H-<sup>1</sup> H spin-spin coupling constants in proteins. In: *NMR in Structural Biology: A Collection of Papers by Kurt Wüthrich*. World Scientific; 1995:114-121.
  20. Schepkin VD, Neubauer A, Nagel AM, Budinger TF. Comparison of potassium and sodium binding in vivo and in agarose samples using TQTPPI pulse sequence. *J Magn Reson*. 2017;277:162-168.  
doi:10.1016/j.jmr.2017.03.003
  21. Fleysher L, Oesingmann N, Inglese M. B<sub>0</sub> inhomogeneity-insensitive triple-quantum-filtered sodium imaging using a 12-step phase-cycling scheme. *NMR Biomed*. 2010;23(10):1191-1198. doi:10.1002/nbm.1548
  22. Fiege DP, Romanzetti S, Mirkes CC, Brenner D, Shah NJ. Simultaneous single-quantum and triple-quantum-filtered MRI of <sup>23</sup>Na (SISTINA). *Magn Reson Med*. 2013;69(6):1691-1696. doi:10.1002/mrm.24417
  23. Burstein D. Stimulated echoes: Description, applications, practical hints. *Concepts Magn Reson*. 1996;8(4):269-278. doi:10.1002/(SICI)1099-0534(1996)8:4<269::AID-CMR3>3.0.CO;2-X
  24. Hahn EL. Spin Echoes. *Phys Rev*. 1948;73(679):580-591.
  25. Kingsley PB. Product operators, coherence pathways, and phase cycling. Part II. coherence pathways in multipulse sequences: spin echoes, stimulated echoes, and multiple quantum coherences. *Concepts Magn Reson*. 1995;7(2):115-136. doi:10.1002/cmr.1820070203
  26. Worthoff WA, Shymanskaya A, Shah NJ. Relaxometry and quantification in simultaneously acquired single and triple quantum filtered sodium MRI. *Magn Reson Med*. 2019;81(1):303-315. doi:10.1002/mrm.27387
  27. Burstein D, Springer Jr CS. Sodium MRI revisited. *Magn Reson Med*. 2019;82(2):521-524. doi:10.1002/mrm.27738

28. Schnurr AK, Chung K, Russ T, Schad LR, Zöllner FG. Simulation-based deep artifact correction with Convolutional Neural Networks for limited angle artifacts. *Z Med Phys*. 2019;29(2):150-161. doi:10.1016/j.zemedi.2019.01.002
29. Lundervold A. Analysis of Texture: Practice. *Proc Intl Soc Mag Reson Med*. 2011;19:19-20. doi:10.2172/4614925

## Supporting Information

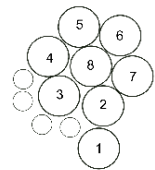


**Figure S.1:** Option I: Original six step phase cycle: (a) shows the three coherence signals contributions over the evolution phase  $\phi_1$  dimension. Circle markers highlight sampling values for phase increment of  $2\pi/6$  and start phase of  $\pi/6$ . (b) Fourier Transform splits the MQC contributions and thus allows to separate the three contributions SQ, DQ and TQ, with TQ signal at the Nyquist horizon.



**Figure S.2:** For better comparison to the simulation data, a single voxel of interest within Phantom 5, 154 mM Na, 5% agar is presented. (a), (b) image data with the voxel of interest marked by a cross. (c) Real and Imaginary parts of the two cycles are plotted along  $\phi_1$  with the circular markers indicating data acquisition. (d,e) spectroscopic result along the multiple echo times. (d) TQ signal can be seen well (e) no visible TQ signal in (e). (f) The data are reconstructed to a total spectroscopic result free of B0 inhomogeneity bias.

**Table S.3:** mean phantom T2\* values, evaluated in a circular ROI of phantom diameter size. The four smaller diameter phantoms were not taken into account and served to see if smaller structures can be resolved.

Phantom Nr. 	Agar (%)	Na (mM)	T2* fast (ms)	T2* slow (ms)	Time of TQ max (ms)	TQ/SQ Ratio (x10 <sup>-2</sup> )*	SQ Signal_TE= 1.15ms (x10 <sup>-5</sup> )**	SQ Fit_TE=0ms (x10 <sup>-5</sup> )***
1	0	154mM	0.9±1.4	22.7±2.7	3.0	1.0±0.2	19.8±0.2	21.3±0.2
2	4	100mM	4.8±0.7	19.6±5.7	9.7	2.9±0.4	11.7±0.2	14.4±0.2
3	4	154mM	5.0±0.6	17.9±2.0	12.8	3.0±0.2	16.1±0.2	19.7±0.2
4	2	130mM	3.7±0.5	25.9±12.0	8.4	1.1±0.2	16.7±0.3	22.6±0.3
5	5	154mM	4.0±1.0	16.6±1.9	12.8	3.1±0.3	16.1±0.2	20.7±0.2
6	4	50mM	4.3±0.5	28.1±8.4	17.0	2.6±0.3	6.6±0.1	8.3±0.1
7	4	100mM	4.7±1.2	17.6±0.8	12.8	2.6±0.3	15.0±0.2	19.7±0.2
8	2	100mM	3.8±2.2	29.2±5.8	15	1.7±0.2	11.7±0.14	13.5±0.2

\*The linear regression model against [Agar] result: R<sup>2</sup> = 0.87 (p-value = 0.0007)

\*\*The linear regression model against [Na] result: R<sup>2</sup> = 0.81 (p-value = 0.0022)

\*\*\*The linear regression model against [Na] result: R<sup>2</sup> = 0.75 (p-value = 0.0058)

#### **S.4 Calculation of zero points in signal equation [1.1] : $\Omega(\text{Hz})=(k\pi+\xi_1)/(2\pi\tau_1)$ :**

Starting from equation 1.1:

$$S(\tau_1, \tau_2, \phi_1, \phi_2, \Omega, TE) = \sum_{p_1} \sum_{p_2} e^{-i(p_1\phi_1+(p_2-p_1)\phi_2)} B_{Na}(p_1, p_2, \tau_1, \tau_2, \Omega, TE, A_{p_1,p_2})$$

[1.1]

$$B_{Na} = e^{-i(p_1\tau_1+p_2\tau_2)\Omega} e^{i\Omega TE} A_{p_1,p_2}$$

$$S(\tau_1, \tau_2, \phi_1, \phi_2, \Omega, TE)/e^{i\Omega TE} = \sum_{p_1} \sum_{p_2} e^{-i(p_1\phi_1+(p_2-p_1)\phi_2)} e^{-i(p_1\tau_1+p_2\tau_2)\Omega} A_{p_1,p_2}$$

$$S(\tau_1, \tau_2, \phi_1, \phi_2, \Omega, TE)/e^{i\Omega TE} = \sum_{p_1} \sum_{p_2} e^{-i((p_1\phi_1+(p_2-p_1)\phi_2)+(p_1\tau_1+p_2\tau_2)\Omega)} A_{p_1,p_2}$$

By factorization:  $((p_1(\phi_1 - \phi_2) + p_2\phi_2) + (p_1\tau_1 + p_2\tau_2)\Omega) = (p_1(\Omega\tau_1 - \xi) + p_2(\phi_2 + \Omega\tau_2))$

Considering the table of the multiple quantum magnitudes:

$\frac{p_2 \rightarrow}{p_1 \downarrow}$	-3	-2	-1	+1	+2	+3
-1	-TQ/4	-DQ/4	-SQ/4	-SQ/4	-DQ/4	-TQ/4
+1	TQ/4	DQ/4	SQ/4	SQ/4	DQ/4	TQ/4

One can consider equivalently all three quanta. We propose the computation for the triple quantum (TQ) but replacing  $p_2 = \pm 3$  with  $p_2 = \pm 2$  or  $p_2 = \pm 1$  will lead to identical results.

$$S_{TQ}(\tau_1, \tau_2, \phi_1, \phi_2, \Omega, TE)/(TQ * e^{i\Omega TE})$$

$$= -e^{-i(-1(\Omega\tau_1-\xi)-3(\phi_2+\Omega\tau_2))} + e^{-i(1(\Omega\tau_1-\xi)-3(\phi_2+\Omega\tau_2))} - e^{-i(-1(\Omega\tau_1-\xi)+3(\phi_2+\Omega\tau_2))} + e^{-i(1(\Omega\tau_1-\xi)+3(\phi_2+\Omega\tau_2))}$$

Writing  $L = e^{i(\Omega\tau_1-\xi)}$  and  $M = e^{i3(\phi_2+\Omega\tau_2)}$  :

$$\frac{4 S_{TQ}(\tau_1, \tau_2, \phi_1, \phi_2, \Omega, TE)}{TQ * e^{i\Omega TE}} = -LM + L^*M - LM^* + L^*M^* = -L(M + M^*) + L^*(M + M^*)$$

$$= (M + M^*)(L^* - L)$$

Thus, signal nulling for all quanta occurs for:

$$L^* - L = 0, \text{ which corresponds to } L = e^{ik\pi} = 1 \text{ for } k \in N_0$$

which corresponds to:  $\Omega\tau_1 - \xi = k\pi$  for  $k \in N_0$

and therefore:  $\Omega_0 = \frac{k\pi+\xi}{\tau_1}$  for  $k \in N_0$  or  $\Omega_0 = \frac{k\pi+\xi}{2\pi\tau_1}$  for  $\Omega$  in Hz.

This result corresponds to equation (21) in Matthies et al.

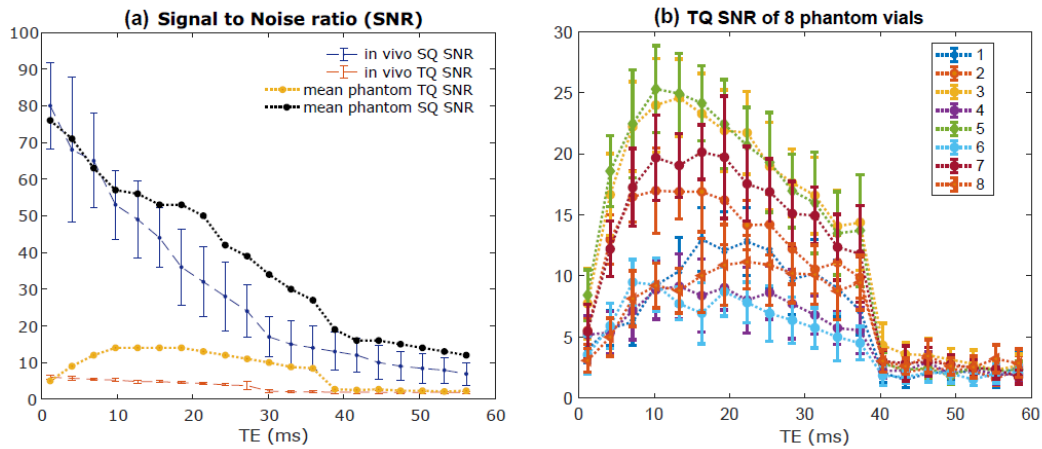


**Figure S6:** Signal to noise ratio (SNR) over echo time, TE. SNR was calculated as the mean signal in the image divided by the standard deviation of the noise region. Image region and noise region were selected with an eroded (image) versus complemented dilated bodymask (noise). To exclude the direct boundary. The in vivo SNR data were averaged over the 5 healthy volunteers. For more details the SNR of the TQimage in the individual vials is given in (b) The sharp falloff at 40 ms resulted from an increase in noise level.

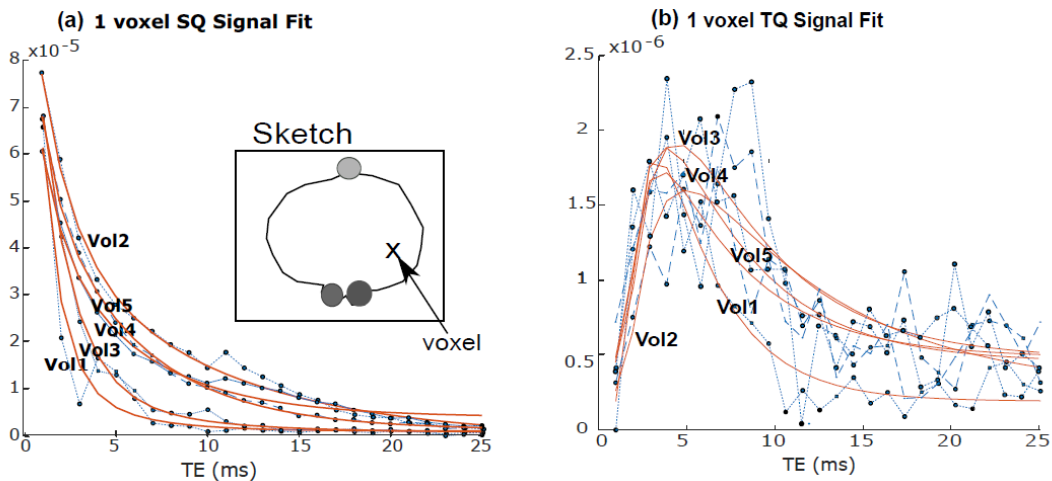


**Figure S7:** An exemplary one voxel fit in the indicated region for each of the 5 volunteers is given. Further development of the fitting routine is necessary to allow the fit in vivo in reasonable time on low SNR images with larger FOV and smaller voxels.